Energy & Environmental Science

ROYAL SOCIETY OF CHEMISTRY

REVIEW

View Article Online
View Journal | View Issue

Cite this: *Energy Environ. Sci.*, 2020, **13**, 3993

Two-dimensional nonlayered materials for electrocatalysis

Yizhan Wang, [a] Ziyi Zhang,[a] Yanchao Mao*[b] and Xudong Wang *[a]

Received 28th May 2020,
Accepted 23rd September 2020

DOI: 10.1039/d0ee01714k

rsc.li/ees

Creating two-dimensional (2D) geometry from nonlayered catalytic materials may significantly advance electrocatalyst design. The 2D morphology of three-dimensional lattices (2D nonlayered materials) offer large structural distortions, massive surface dangling bonds, and coordinated-unsaturated surface atoms, which can induce high surface chemical activity and promote the chemisorption of reactants and fast interfacial charge transfer, thereby enhancing the electrocatalytic performance. In this article, we review typical strategies for structural engineering and manipulation of electronic states to enable the unique electrocatalytic advantages of 2D nonlayered materials. An overview is presented on recent research advances in the development of 2D nonlayered materials for catalyzing the representative electrochemical reactions that are essential to energy and sustainability, including hydrogen evolution, oxygen evolution, oxygen reduction, and CO_2 reduction. For each type of redox reactions, their unique catalytic performance and underlying mechanism are discussed. Important achievements and key challenges are also discussed.

Broader context

Due to their unique and exotic structural and electronic properties, great progresses have been made in syntheses and applications of two-dimensional (2D) nanostructures with nonlayered materials over the past decade. This paper provides a comprehensive overview on the recent research advances in the development of 2D nonlayered materials for representative electrochemical reactions that are essential to energy and sustainability, including hydrogen evolution, oxygen evolution, oxygen reduction, and CO_2 reduction. Further, 2D nonlayered materials offer several unique structural and catalytic advantages, including higher density of low-coordinated surface atoms, massive surface dangling bonds, large lattice distortions, and rich defects. Together, these features offer great benefits for improving surface chemisorption, tuning the surface electronic states, enhancing carrier mobility, and enabling fast reaction kinetics. Moreover, 2D nonlayered materials will soon evolve into a new group of highly efficient, cost-effective, and sustainable electrocatalysts for a broad range of energy and environmental applications.

1. Introduction

Two-dimensional (2D) nanomaterials have attracted extensive research interests in recent years and are now playing a key role in materials innovation and property advancement.[1–4] The family of 2D nanomaterials has rapidly expanded from graphene to carbon nitrides,[5–14] transition metal dichalcogenides (TMDs),[15] Xenes,[16] black phosphorus (BP),[17] hexagonal boron nitride,[18] metal–organic frameworks (MOFs),[19] and their heterostructures.[20,21] In contrast to their bulk counterparts and other forms of nanostructures, 2D nanomaterials—with thickness of just one or a few atomic layers—can afford unique optical, electrical, chemical, and mechanical properties, leading to broad application potential in photovoltaics, catalysts, sensors, and thermoelectrics.[4,22–24] Until now, the study of 2D nanostructures has been largely limited to naturally layered materials, *i.e.*, van der Waals (vdW) solids. These solids have strong in-plane chemical bonds but weak out-of-plane vdW bonds, and therefore, they can be readily produced either from top-down methods (such as exfoliation by micromechanical cleavage,[25] ionic intercalation in solution,[26] and ultrasonication[27]) or from bottom-up methods (such as chemical vapor deposition[3,28,29]). Their 2D atomic lattices give rise to ultrahigh specific surface area, enhanced electronic conductivity, and short electron/carrier transfer distance. These intriguing structural and electronic properties of 2D nanomaterials result in numerous potentials for electrocatalysis applications. Currently, a broad range of 2D nanomaterials as advanced electrocatalysts have been comprehensively discussed in a number of review articles.[30–34]

Nevertheless, many traditional high-performance electrocatalysts, such as precious metals (*e.g.*, Pt, Pb) and metal oxides

[a] *Department of Materials Science and Engineering, University of Wisconsin-Madison, Madison, WI 53706, USA. E-mail: xudong.wang@wisc.edu*
[b] *Key Laboratory of Materials Physics, Ministry of Education, School of Physics and Microelectronics, Zhengzhou University, Zhengzhou 450001, China. E-mail: ymao@zzu.edu.cn*

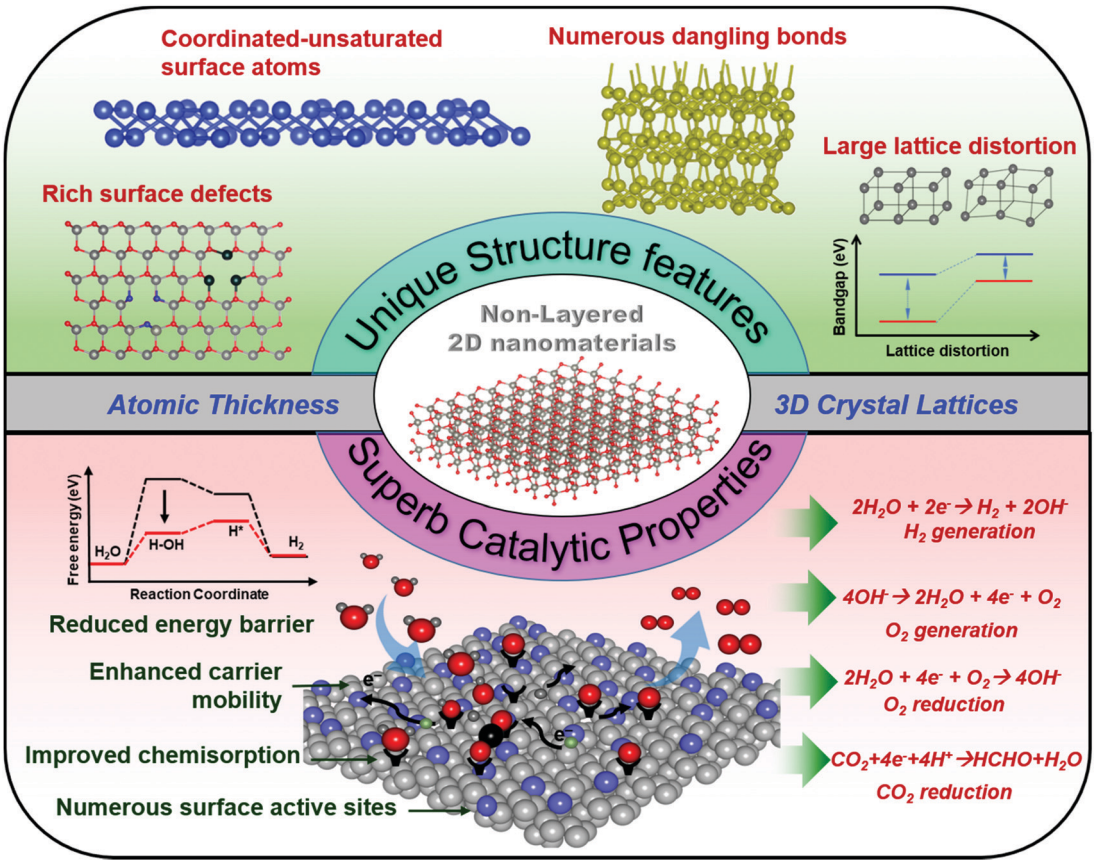

Fig. 1 Unique structural features and associated superb catalytic properties of 2D nonlayered materials for their applications toward HER, OER, ORR, and CO_2 reduction reaction.

(*e.g.*, RuO_2, IrO_2), have a nonlayered crystal structure with intrinsic isotropic chemical bonds in three dimensions. Compared with vdW solids, creating 2D geometry from these nonlayered catalytic materials may offer higher impacts toward catalyst design (Fig. 1). First, the 2D nonlayered materials may be subject to large structural distortion with massive surface dangling bonds, which is not common in layered materials; this enables highly chemically active surfaces and enhanced catalytic performance. Second, the exposed surface atoms with low coordination numbers can promote the chemisorption of reactants and induce faster interfacial charge transfer. Third, the structural and electronic properties of 2D nonlayered materials can be tuned by structural and surficial engineering, which can further tailor the catalytic performance. Moreover, defects (*e.g.*, vacancies) are always associated with 2D lattices, which offer additional influences to the surface electronic structure and charge transport properties. Fundamentally, ultrathin 2D geometry provides an ideal and relatively simple platform to study the catalytic mechanisms at the atomic level, as well as to model the electronic-state modulation for establishing reliable structure–property relationships.

Different from 2D vdW solids, the creation of 2D morphology from nonlayered materials typically requires the stabilization of crystal phases or structures far away from thermodynamic equilibrium. The control of kinetics must be introduced to break the crystal symmetry and foster 2D anisotropy in crystal growth. To realize the anisotropic growth of nonlayered materials, a number of strategies for synthesizing 2D morphology from a broad range of materials—beyond those bonded by vdW interactions—have been developed, such as ionic layer epitaxy (ILE),[35] oriented attachment,[36] lamellar intermediate-assisted exfoliation,[37,38] 2D template synthesis,[39] and topochemical transformation.[40] Based on these novel synthesis strategies, a broad range of 2D nonlayered materials have been successfully developed, such as metals, metal oxides, metal chalcogenides, TMDs, metal nitrides, metal phosphides, and many others.[41] Due to the absence of an intrinsic layered configuration, these materials usually exhibit a thickness of at least a few layers of unit cells (*i.e.*, in the range of 0.5 nm to >10 nm). Therefore, they should be more accurately termed as quasi-2D nanomaterials. To make it simple, in this article, all of them are termed as 2D nonlayered materials or they are followed by specific material names. Representative synthesis strategies for 2D nonlayered materials have been well documented in a few recent reviews.[1,41,42] Based on the blooming of various 2D nonlayered materials, promising results have also been demonstrated in advancing electrocatalysis applications by this new family of 2D nanomaterials. Nevertheless, despite the remarkable initial successes in 2D nonlayered materials for electrocatalysis, there is a lack of comprehensive reviews focusing on the promising catalytic

behavior related to the 2D lattices of nonlayered materials. In this article, we will provide a systematic overview of recent research advances in the development of 2D nonlayered materials for electrocatalysis applications. First, we will introduce strategies for the structural engineering and manipulation of electronic states of 2D nonlayered materials, enabling their unique advantages as electrocatalysts. Thereafter, we will discuss the applications of 2D nonlayered materials for catalyzing four representative categories of electrochemical reactions that are essential to energy and sustainability, namely, hydrogen evolution reaction (HER), oxygen evolution reaction (OER), oxygen reduction reaction (ORR), and CO_2 reduction reaction. For each reaction, their unique catalytic performance and underlying mechanism will be described. At last, we will conclude with a summary of the important achievements and an outlook on the key challenges in this field.

2. Structural engineering of 2D nonlayered electrocatalysts

The intriguing advantages of 2D nanomaterials for electrocatalysis are primarily related to their unique morphology and atomic structures. In this section, we will discuss how to control a few key parameters of 2D nonlayered materials, such as thickness, point defects (vacancies and doping), and heterogeneity, as well as their influences on electrocatalysis applications.

2.1. Thickness control

Controlling the thickness of the material down to the nanometer scale is one of the most effective ways to modulate the electronic structure and chemical activities. When the thickness of a semiconductor material is reduced to a few or a single atomic layer, its bandgap broadens due to the quantum confinement effect. The electronic density of state (DOS) can also largely increase at the surface of a 2D material compared with those in the interior of a bulk structure. In addition, the reduced thickness could induce surface lattice distortion[43] and changes in the electronic structure (such as lowering the work function), indicating the potential to achieve tunable band alignment in electrocatalysis design.[44] Furthermore, the ratio of the exposed surface atoms sharply increases as the thickness reduces to the nanometer scale, leading to an enhanced surface effect. Due to the lack of neighboring atoms, abundant low-coordination surface atoms with dangling bonds are formed. To maintain structural stability, these surface atoms are prone to bonding with other atoms or molecules and therefore show much improved chemical activity.[32] In a representative example, the catalytic performance of 2D SnO_2 with different thicknesses was compared with respect to carbon monoxide (CO) oxidation.[45] Because subnanometer-thick 2D SnO_2 had a larger fraction of low-coordination surface atoms and higher DOS compared with thicker SnO_2 nanosheets and bulk SnO_2, it exhibited remarkably improved CO catalytic performances, with the activation energy lowered from 121.1 to 59.2 kJ mol^{-1} and full CO conversion temperature reduced by over 200 °C.

Nevertheless, different from layered crystal structures, where the thickness can be relatively easily controlled by the number of atomic layers, controlling the thickness of 2D nonlayered materials is rather challenging due to the lack of a significant driving force for 2D anisotropic growth. In the 2D SnO_2 catalysts mentioned above, the thickness was controlled by the growth temperature. Further, 2D SnO_2 with an average thickness of 0.66 nm were synthesized at 180 °C for 48 h in a solvothermal reaction between $SnCl_2{\cdot}2H_2O$ and ethylenediamine. A higher temperature of 220 °C yielded a larger average thickness of ~1.9 nm.[45] This is a relatively common growth phenomenon in which a higher temperature leads to faster growth rate and therefore weakens the anisotropy in 2D morphology.[46] In wet-chemistry systems, the concentration of precursors was also found to control the thickness. Typically, higher precursor concentrations can promote more isotropic growth of 2D materials, leading to larger thickness after the possible Ostwald ripening process (Fig. 2a and b).[47–49] By considering the example of a graphene-oxide-templated synthesis strategy, a range of binary oxides (*e.g.*, MgO, ZrO_2, Al_2O_3, TiO_2, SnO_2, and Sb_2O_5) were grown into 2D morphology with a thickness of several nanometers. The thickness of these 2D layered materials could be tuned by the concentration of the metal precursors.[50]

Despite the possibilities of a wide range of thickness control strategies by varying the reaction conditions, the tuning of the thickness of 2D nonlayered materials down to a single atomic layer has been rarely reported. One technology that distinguishes itself from others with the capability of unit-cell-level thickness control is the ILE technique. It was recently developed as an effective strategy to synthesize 2D nonlayered materials, such as ZnO,[35,51] Pd,[52] and CoO,[53,54] which are promising electrocatalysts. In this technology, surfactant monolayers are used as a soft template at the water–air interface to guide the growth of 2D materials; here, it was found that the packing density of the surfactant was the key parameter for thickness control. Based on the example of 2D ZnO growth systems, molecular dynamics (MD) simulations revealed that both Zn^{2+} concentration and width of the Zn^{2+}-concentrated zone (the Stern layer) underneath the surfactant monolayer increased monotonically with an increasing surfactant packing density (Fig. 2c). By comparing the experimental measurements with the simulation results, an excellent match between the thickness and Stern layer width could be observed, confirming the direct relationship between the thickness of the Stern layer and thickness of the 2D materials (Fig. 2d). As the surface pressure was adjusted from 3.09 to 16.40 mN m^{-1}, 2D ZnO with one- to four-unit-cell thickness could be achieved (Fig. 2e). This self-limited thickness control in ILE brings up a new capability for the precision thickness control of 2D nonlayered material synthesis, which may enable a more comprehensively quantitative study on 2D electrocatalysis.

2.2. Vacancy manipulation

Cation and anion vacancies are a well-known factor that controls the physical and catalytic properties of materials, such as

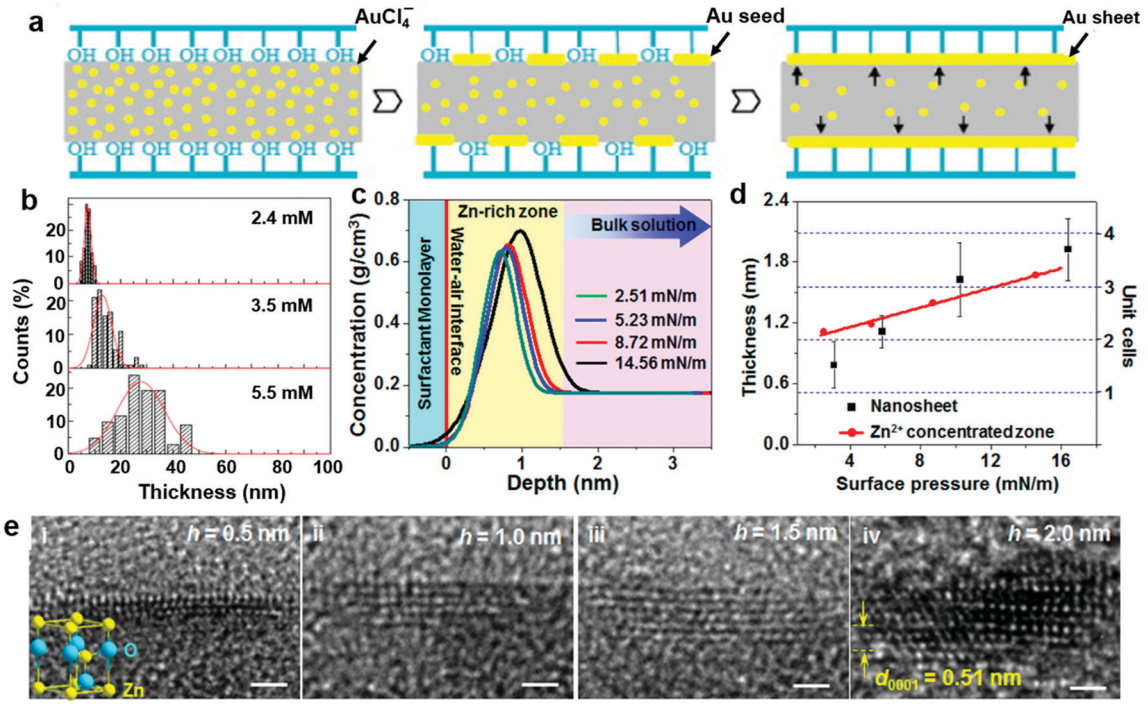

Fig. 2 Thickness control of 2D nonlayered materials. (a) Schematic of the synthesis of 2D Au. (b) Thickness distribution histograms corresponding to different $HAuCl_4$ concentrations.[47] Reproduced with permission from © 2013 American Chemical Society. (c) Zn^{2+}-ion concentration profiles underneath the surfactant monolayer with four different surface pressures. Sky blue represents the surfactant monolayer. Light yellow represents the Zn-concentrated zone (the Stern layer). Lavender represents the bulk solution. (d) Plots of the thickness (black squares) and width of Zn-concentrated zone (red dots) as functions of the surface pressure. The numbers of ZnO unit cell are highlighted by dashed blue lines. (e) Cross-sectional HRTEM images of 2D ZnO with a thickness from one to four unit cells. Inset shows one unit cell of wurtzite ZnO.[44] Reproduced with permission from © 2017 American Chemical Society.

electronic structure, carrier concentration, electrical conductivity, and atom coordination. As a result of the intrinsic 3D crystal lattices, vacancies are commonly found in 2D nonlayered materials, and they might have significant impacts on the catalysis performance. For example, Sn/O dual vacancies in 2D SnO_2 could evolve into an isolated Sn vacancy under a relatively small electric field, which can induce a reversible transition between the semiconductor and half metal accompanied by an abrupt conductivity change of up to 10^3 times. DFT calculations further revealed that 2D SnO_2 with Sn/O dual vacancies show semiconductive behavior; an isolated Sn vacancy can induce a half-metallic characteristic, mostly originating from the O 2p state.[55,56] The DFT calculation also revealed that the presence of O vacancies in 2D In_2O_3 could increase the DOS at the valence band edge and lead to a new defect level in the forbidden band (Fig. 3a and b).[57] The change in the electronic structure suggested that electrons could be more easily excited into the conduction band, and therefore, the O-vacancy-rich 2D In_2O_3 showed a higher carrier concentration than that of a perfect lattice. In addition, the physicochemical properties can also be tailored by vacancies. It was reported that Co vacancies in 2D $CoSe_2$ could serve as active sites to catalyze OER (Fig. 3c and d).[58] DFT calculations showed that Co vacancies in 2D $CoSe_2$ exhibited a water-molecule adsorption energy of 0.85 eV, larger than that of cobalt sites in bulk $CoSe_2$ (0.38 eV); this indicated that Co vacancies in an ultrathin structure could be more favorable for adsorbing H_2O and catalyzing OER.

Commonly, vacancies can be created and tuned in multiple ways in bulk crystals, where most of them can be readily adapted to 2D nonlayered materials. Fast-heating phase transformation is a powerful approach to engineer surface defects.[57,59–61] As a typical example, starting with ultrathin $In(OH)_3$, fast heating at 400 °C for 3 min affords 2D In_2O_3, where the concentration of O vacancies was controlled by the oxygen partial pressure of the calcination atmosphere.[57] As a kinetically controlled synthesis approach, the ILE technique is also versatile in controlling the evolution of defects within a quasi-2D crystal lattice. By introducing a water–oil interface, polycrystalline 2D ZnO with an unprecedented Zn vacancy concentration of ~33% could be synthesized (Fig. 3e and f). Stabilizing such a high Zn-vacancy concentration could be attributed to the local charge balancing in the ultrathin geometry from the surfactants and fast growth kinetics.[62] In addition, plasma treatment has been demonstrated as an efficient strategy to introduce surface vacancies. For example, Ar plasma on 2D Co_3O_4 could partially reduce Co^{3+} to Co^{2+}, producing O vacancies. The synergistic effect of the surface O vacancies and high surface area of 2D Co_3O_4 could largely enhance the electrocatalytic activity.[63]

2.3. Elemental doping

Extrinsic point defects, represented by elemental dopants, can result in many intriguing physical and chemical alterations, such as distortion in atomic arrangement, redistribution of electron density, higher number of delocalized electrons, and exposure of more active sites, providing opportunities to manipulate 2D

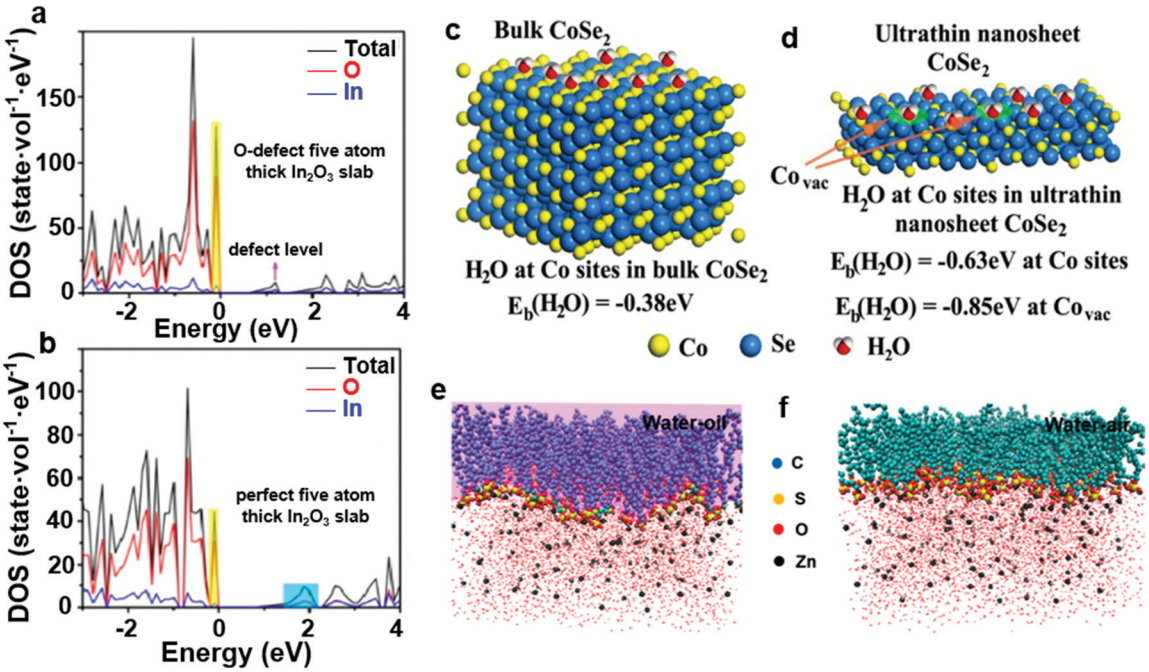

Fig. 3 Vacancy manipulation of 2D nonlayered materials. (a) Calculated DOS of oxygen-defect five-atom-thick In_2O_3 slab. (b) Calculated DOS of perfect five-atom-thick 2D In_2O_3.[57] Reproduced with permission from © 2014 American Chemical Society. First-principles study of surface H_2O adsorption on different sites and performance of various materials. (c and d) Geometries and binding energies of H_2O molecules on cobalt sites and vacancies.[58] Reproduced with permission from © 2014 American Chemical Society. MD-simulation-generated Zn^{2+}-ion distribution at the (e) water–air and (f) water–oil interfaces.[62] Reproduced with permission from © 2019 American Chemical Society.

materials for enhanced catalytic applications. For instance, Zhang *et al.* effectively regulated the electronic structure of 2D Ru and enhanced the HER activity by Al doping.[64] DFT calculations showed that the basal plane of Al-doped 2D Ru exhibited more delocalized electron distribution than pristine 2D Ru, raising the number of active sites on 2D Ru for HER (Fig. 4a). Besides, more states at the valence band edges could accelerate electron transfer from the catalyst surface to the adsorbed H^+, facilitating the reduction reaction. Further, Al doping reduced the Gibbs free energy for hydrogen adsorption (ΔG_{H^*}), thereby improving the catalytic performance.

Confined doping in atomic layers has been recently reported as an effective approach in moderating the catalytic properties of 2D nonlayered materials. Here, doping elements are confined in the basal planes of the material while maintaining the 2D atomic arrangement and electron conjugated system. This strategy could yield an excess of catalytic active sites, providing an opportunity to regulate the electronic structure to optimize the electrocatalytic dynamics. Confined Co doping in three atomic layers of In_2S_3 brought several new energy levels due to the splitting of the Co 3d states, thereby affording significant improvements in the photocatalytic activity.[65] DFT calculations showed that a vast majority of charge density originated from the Co and S atoms (Fig. 4b), suggesting that most of the confined Co dopants were directly involved in the photocatalytic reaction and therefore facilitated easier electron excitation by the d–d internal transitions of Co ions under light. The presence of Co dopant also endowed 2D In_2S_3 with obviously increased DOS at the conduction band minimum, which allowed for higher carrier density and efficient carrier transport along the 2D conducting channels. Through a similar approach, Mn was doped into the primitive lattice of 2D $CoSe_2$, introducing subtle atomic distortion and heterogeneous spin states in the atomically thin lattices (Fig. 4c).[66] The variation in the electronic structure could lower the kinetic energy barrier by promoting H–H-bond formation on two adjacently adsorbed H atoms and therefore enhanced the HER performance.

In general, this section summarizes three important and unique structural factors, *e.g.*, thickness, intrinsic defects (vacancies), and extrinsic defects (dopants) in 2D nonlayered materials; further, we discuss how they can be controlled and fundamentally correlated to the catalytic performance. In the following sections, we will discuss specific examples of 2D nonlayered materials revealing how their ultrathin geometry is correlated to four representative catalytic processes, *i.e.*, HER, OER, ORR, and CO_2 reduction reaction.

3. HER

The hydrogen fuel cell is a critical technology in clean and renewable energy applications. Electrocatalytic water splitting is the main source of high-purity hydrogen, where the HER is the cathodic reaction in water electrolysis producing H_2. The thermodynamic potential needed to drive water electrolysis is 1.23 V (*vs.* a reversible hydrogen electrode (RHE)), while the practical voltage applied to drive water electrolysis is usually larger than this value due to the Ohmic drop and overpotential associated with reactions on the anode and cathode. HER is a

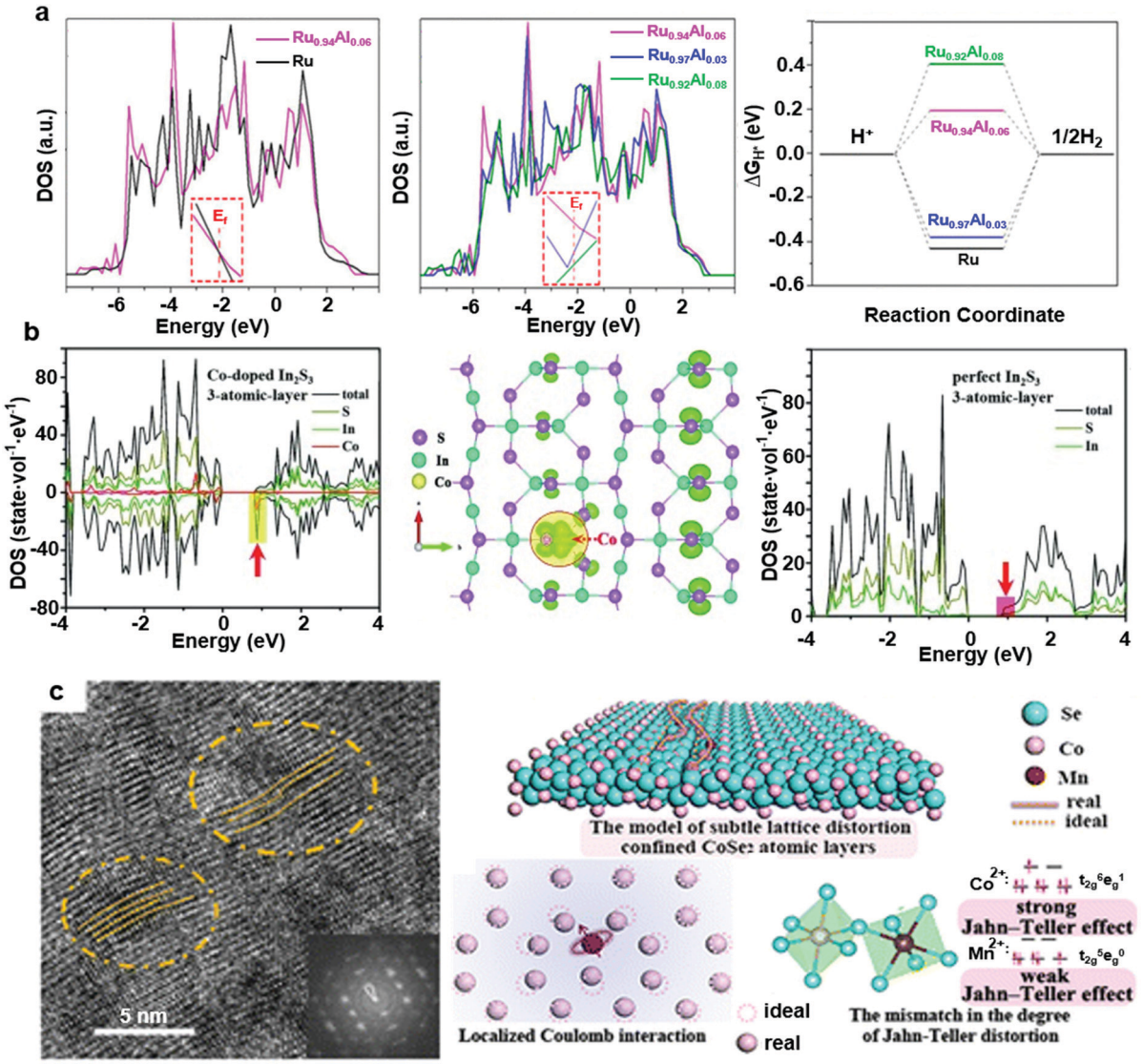

Fig. 4 Elemental doping of 2D nonlayered materials. (a) DFT-calculated DOSs and HER free-energy diagrams of pristine and Al-doped 2D Ru.[64] Reproduced with permission from © Copyright 2019 American Chemical Society. (b) DFT-calculated DOSs and charge-density distribution of the conduction band edge of Co-doped and pristine 2D In_2S_3 with three-atomic-layer thickness.[65] Reproduced with permission from © 2015 Wiley-VCH Verlag GmbH & Co. KGaA, Weinheim. (c) HRTEM images and corresponding FFT patterns (insets) for Mn-doped 2D $CoSe_2$ with schematic representations of the formation mechanism for the subtle distortion of atomic arrangement through the incorporated heterogeneous spin states.[66] Reproduced with permission from © Copyright 2016 American Chemical Society.

two-electron transfer reaction with multiple steps, namely, adsorption, reduction, and desorption. The adsorption of hydrogen (H*) on the catalyst surface typically occurs *via* the Volmer process, which is then reduced, forming molecular hydrogen *via* either a Heyrovsky or Tafel step.[30] During HER, the hydrogen adsorption energy typically plays the most significant role in determining the rate of the overall reaction, and it is the key factor in catalyst development.[56] HER catalysis is one of the most promising applications for 2D nonlayered materials that show catalytic activities comparable to those of Pt-based catalysts. As a high-performance catalytic material, they share many common advantages such as very large surface area, numerous low-coordinated atoms for hydrogen adsorption, and improved electrical conductivity and carrier mobility. These advanced features could be further tuned to enhance the electrocatalytic performances by engineering the material structure. So far, a variety of 2D nonlayered materials have been studied for HER electrocatalysis, such as metals, transition metal chalcogenides (TMCs), metal phosphides, and metal nitrides. In contrast, 2D layered materials, such as graphene and TMDs, intrinsically show relatively low activity toward the HER electrocatalysis due to their mostly coordinated surface. The basal plane of pure graphene is inert toward HER with a relatively large (positive) ΔG_{H^*} (1.85 eV). To improve the HER performance, elements with different electronegativities, such as N, P, and S, have to be doped into the carbon matrix of graphene to induce the redistribution of charge/spin to the graphene layer. For layered TMDs, the HER performance is largely limited by the density of the active sites, which are concentrated at

the layer edges. Accordingly, significant research efforts have been directed toward synthesis strategies that can expose additional active edge sites to enhance the overall performance. Strategies such as heteroatom doping, defect engineering, interaction engineering, *etc.* have been used to tune the ΔG_{H^*} and band structure for enhanced activity. A summary of different 2D nonlayered catalysts and their characteristic parameters reported for HER is provided in Table 1. Here, we will discuss the advanced HER performance of 2D nonlayered materials in these material groups together with the representative strategies that can be used to improve their performance.

3.1. Metals

A number of noble metals are well-known excellent catalytic materials for HER. However, their strong preference for close-packed crystalline structures and rich dangling bonds would make 2D metal materials extremely active and unstable.[67] Therefore, the synthesis of 2D metals remains a formidable challenge, although the 2D morphology is expected to afford extraordinary catalytic properties.[68,69] Kong *et al.* used a solvothermal method to synthesize free-standing 2D Ru with a thickness of 1.0–1.2 nm *via* oriented attachment. In this approach, isopropanol was used as the solvent to guide anisotropic Ru growth. Meanwhile, urea was introduced as the selective capping reagent to prevent colloidal aggregation and direct the attachment into large 2D geometry (Fig. 5a).[70] The 2D structure exhibited enhanced HER activities compared with the Ru powder counterparts (Fig. 5b), with onset potential comparable to the value for commercial Pt/C. The overpotential was reduced to 20 mV at a current density of 10 mA mg^{-1} and Tafel slope of 46 mV dec^{-1}. DFT calculations

Table 1 Summary of 2D nonlayered materials reported for HER electrocatalysts

Catalyst	Electrolyte	Synthetic method (precursor)	Thickness	Overpotential (mV) (10 mA cm^{-2})	Tafel slope (mV dec^{-1})	Ref., year
Ru	0.5 M H_2SO_4	Solvothermal method with $Ru(acac)_3$ and urea	1.0–1.2 nm	20	46	70, 2016
Ni	0.1 M KOH	Topotactic reduction of $Ni(OH)_2$	2.2 nm	Onset potential of 34 mV	114	71, 2016
Pt/Cu	0.05 M H_2SO_4	CO-assisted method with $Pt(acac)_2$, $Cu(acac)_2$ and PVP	1.6 nm	55 (100 mA cm^{-2})	23	72, 2016
Ni–Mo alloy	1.0 M KOH	Topotactic reduction of $NiMoO_4$	2 nm	35	45	73, 2017
PtAgCo	0.5 M H_2SO_4	Oxidative etching strategy with $Co(acac)_2$ $Pt(acac)_2$, and $AgNO_3$	—	705 mA cm^{-2} at −400 mV	27	74, 2017
PdCu alloy	1.0 M KOH	CO-assisted method with Na_2PdCl_4 and $CuCl_2$	1.8 nm	106	124	75, 2017
$NiSe_2$	0.5 M H_2SO_4	Topotactic conversion with β-2D $Ni(OH)_2$, Se powder and $NaBH_4$.	—	135	37	76, 2015
Ultra-thin Fe–Ni–S	0.5 M H_2SO_4	Topotactic conversion from FeNi layered double hydroxide (LDH)	2 nm	105–117	40–48	77, 2015
$NiCo_2S_4$	1.0 M KOH	Sulfidation of NiCo-LDH	10–15 nm	65	84.5	78, 2016
Mn-Doped $CoSe_2$	0.5 M H_2SO_4	Conventional liquid exfoliation of Mn-incorporated $CoSe_2$/DETA	1.2 nm	195	36	66, 2016
Se-Enriched $NiSe_2$	H_2SO_4 pH ~ 0.67	Vapor selenization of $Ni(OH)_2$	—	117	32	79, 2016
Co_3S_4	1.0 M KOH	Plasma-assisted conversion of Co_3S_4/triethylenetetramine	1 nm	63	58	80, 2018
NiSe	1.0 M NaOH	Topotactic transformation strategy with $Ni(OH)_2$/NaHSe	1.25 nm	177	58.2	81, 2018
Ni_3N	0.5 M H_2SO_4	Simple sintering process with $Ni(CH_3CO_2)_2{\cdot}4H_2O$ and urea	—	100 (100 mA cm^{-2})	59.79	82, 2016
Mo_5N_6	1 M KOH	Ni-Induced salt-templated method	3 nm	94	66	83, 2018
CoP	0.5 M H_2SO_4	Phosphidation of α-$Co(OH)_2$	—	90	43	84, 2014
Ni_5P_4–Ni_2P	0.5 M H_2SO_4	Phosphorization of commercially available nickel foam	—	120	79.1	85, 2015
Mo–W–P	0.5 M H_2SO_4	Phosphidation of molybdenum tungsten oxide	—	93 (20 mA cm^{-2})	52	86, 2016
MoP	0.5 M H_2SO_4	Phosphidation of MoS_2	—	124	58	87, 2016
FeCoP	1 M KOH	Phosphidation of CoFe-LDH	1.1 nm	188 (100 mA cm^{-2})	76	88, 2017
CoP	0.5 M H_2SO_4	Phosphidation of 2D Co_3O_4	1.1 nm	56	44	89, 2017
CoP	0.5 M H_2SO_4, 1 M KOH, and 1 M PBS	Phosphatization of 2D Co_3O_4 aerogel with $NaH_2PO_2{\cdot}2H_2O$	<1.5 nm	113 (H_2SO_4) 154 (KOH) 161 (PBS)	67 (H_2SO_4) 72 (KOH) 81 (PBS)	90, 2018
Co_2P	0.5 M H_2SO_4	Salt-templating method with $Co(NO_3)_2{\cdot}6H_2O$ and $(NH_4)_2HPO_4$	4 nm	41	35	91, 2018
FeP	0.5 M H_2SO_4	Phosphidation of γ-Fe_2O_3 with NaH_2PO_2 at 320 °C	0.7 nm	95	41	92, 2019
Mo-Doped CoP	1 M KOH	Phosphidation of Mo-Co(OH)F with NaH_2PO_2 at 300 °C	10–15 nm	49	80	93, 2019
N,P-graphene[a]	0.5 M H_2SO_4	Porous-metal-based chemical vapor deposition	—	344	118	94, 2019
S-Doped C_3N_4[a]	0.5 M H_2SO_4	Polycondensation of trithiocyanuric acid,	0.325 nm	186	84	95, 2017
S-Vacancies and edge-rich MoS_2[a]	0.5 M H_2SO_4	Lithiation, desulfurization, and exfoliation	~1.5 nm	153	43	96, 2016
WSe_2[a]	0.5 M H_2SO_4	Mechanically exfoliation	~1 nm	245	76	97, 2016
Edge-rich MoS_2/$Ni(OH)_2$ hybrid[a]	1 M KOH	Liquid exfoliation and cathodic electrodeposition process	—	57	30	98, 2020

[a] Representative 2D layered materials for comparison.

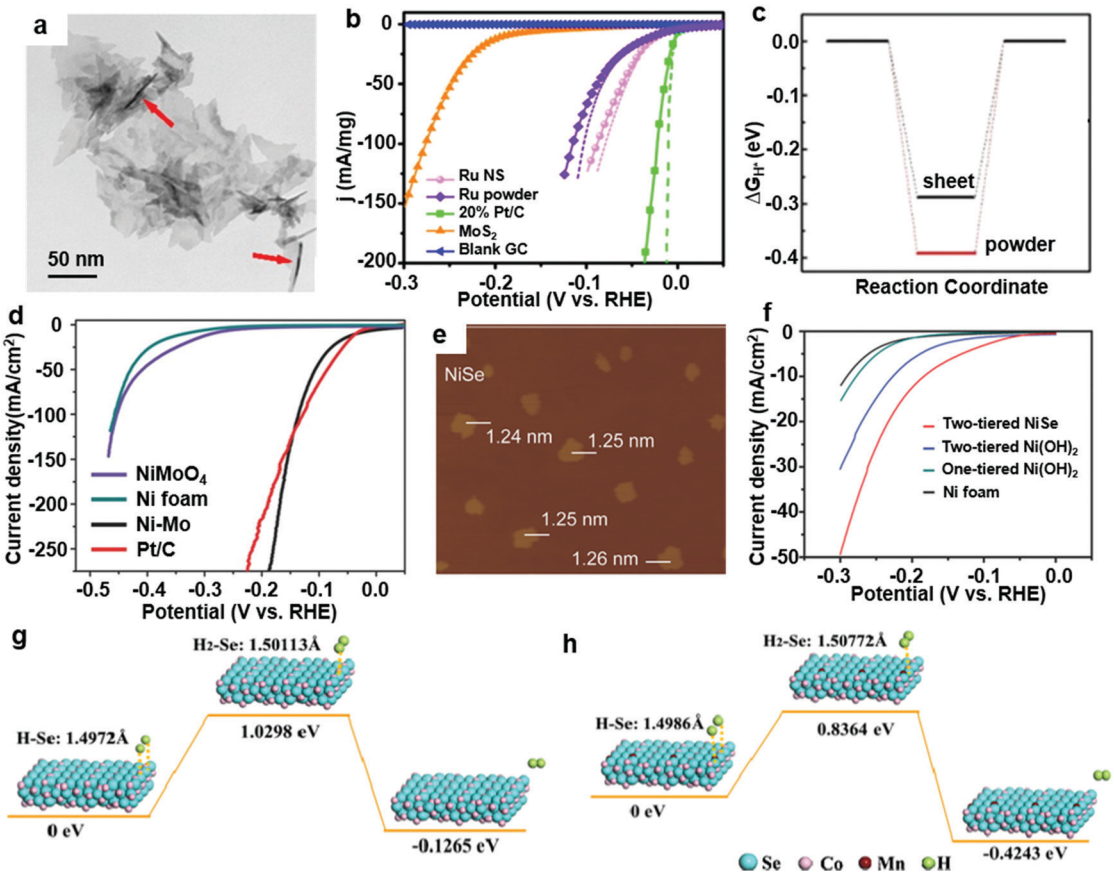

Fig. 5 Different types of 2D nonlayered materials for HER. (a) TEM of the as-synthesized 2D Ru. (b) LSV of 2D Ru in HER in 0.5 M H_2SO_4 electrolyte at pH 0. (c) HER free-energy diagram calculated at the equilibrium potential for 2D Ru and powder surfaces.[70] Reproduced with permission from © Copyright 2016 American Chemical Society. (d) Polarization curves of 2D Ni–Mo (0.8 mg cm^{-2}), Pt/C (1.6 mg cm^{-2}) powder, $NiMoO_4$ precursor, and Ni foam in 1 M KOH.[73] Reproduced with permission from © 2017 Wiley-VCH Verlag GmbH & Co. KGaA, Weinheim. (e) AFM images of 2D NiSe. (f) HER LSV curves of two-tiered NiSe, two-tiered $Ni(OH)_2$, and one-tiered $Ni(OH)_2$ 2D materials, as well as bare Ni foam.[81] Reproduced with permission from © 2018 Wiley-VCH Verlag GmbH & Co. KGaA, Weinheim. (g and h) Kinetic-energy-barrier profiles of HER on the edge sites of virgin $CoSe_2$ and Mn-doped 2D $CoSe_2$, respectively.[66] Reproduced with permission from © Copyright 2016 American Chemical Society.

indicated that the enhanced HER activity from 2D Ru could be attributed to the smaller free-energy change ($|\Delta G_H|$) for hydrogen adsorption at the hollow sites on Ru(001) (Fig. 5c). Nevertheless, surface-capping ligands have always been undesirable as they block the sites or routes for hydrogen adsorption. To realize nonligand-capped 2D metal materials, Kuang *et al.* reported an *in situ* topotactic reduction method to synthesize 2.2 nm 2D nickel arrays from $Ni(OH)_2$. The partial oxidization of 2D Ni resulted in impressive HER activities with a Tafel slope of 114 mV dec^{-1}, smaller than that of the Ni/NiO nanoparticles counterpart (135 mV dec^{-1}).[71]

To improve the HER kinetics on a metal surface, great efforts have been focused on metal alloying. Well-defined alloys often exhibit better catalytic properties than their monometallic counterparts due to the synergistic catalytic effect[72] and the evolution of the surface electronic state.[73] In metal alloys, the mutual pairing and sharing of d-orbital electron can tune the electronic configurations that are suitable for proton adherence and transference.[99] Metikoš-Hukovic *et al.* reported that the Ni–Zr alloy exhibited a rapid increase in the DOS of the Ni 3d orbitals at the Fermi level, which consequently led to a weaker bond of M–H_{ads} and higher HER activity.[100] The synergistic effect of metal alloying and 2D geometry could further enhance the electrocatalytic activity. Furthermore, 2D materials obtained from the metal alloys of Pt–Cu,[72] Ni–Mo,[73] Pt–Ag–Co,[74] Pd–Cu,[75] and Ru–Pd–Ni[101] have been studied for their HER performances. Zhao *et al.* found out that 1.8 nm-thick 2D Pd–Cu alloy only needed overpotential of 106 mV to achieve an HER current density of 10 mA cm^{-2} in alkaline media; however, 2D Pd needed overpotential of 235 mV to reach the same current density.[75] Zhang *et al.* reported the electrocatalytic HER by 2D nonnoble Ni–Mo alloy synthesized by the *in situ* topotactic reduction of $NiMoO_4$ precursors.[73] Introducing Mo into Ni could modify the electron DOS of the d orbitals and therefore change the ΔG_H value on the metal surface.[102] 2D Ni–Mo with a thickness of 2.0–2.1 nm showed overpotential of 35 mV at a current density of 10 mA cm^{-2} (Fig. 5d), along with a Tafel slope of 45 mV dec^{-1}, affording catalytic activity comparable to that of the commercial Pt/C catalyst. Besides, 2D Ni–Mo showed faster mass transfer behavior at a higher current density compared with that of the Pt/C catalyst. Based on these impressive initial successes, it can be argued that 2D metal alloys can prove to be a

promising new solution for developing low-cost, highly efficient, nonnoble-metal-based HER catalysts.

3.2. TMCs

TMCs have been studied as HER catalysts because of their predicated low ΔG_H values[103] as well as their low cost and high stability. Typically, 2D nonlayered TMCs are prepared by the topotactic conversion of layered precursors. Different 2D TMCs such as $NiCo_2S_4$,[78] $NiSe_2$,[76,79] NiSe,[81] NiS,[77] $Ni_{1-x}Fe_xPS_3$,[104] $CoSe_2$,[66] and Co_3S_4[80] have been synthesized and studied for HER applications. Wu *et al.* prepared ~1.25 nm 2D NiSe from 2D $Ni(OH)_2$ precursors (Fig. 5e) and studied the full water electrolysis.[81] Further, 2D NiSe showed improved HER performance with lower onset overpotential (177 mV at 10 mA cm^{-2}) and smaller Tafel slope (58.2 mV dec^{-1}) compared with those of layered $Ni(OH)_2$ (Fig. 5f). This improvement can be attributed to the largely exposed catalytically active Se sites on the 2D structure, as the free energy for hydrogen adsorption was much lower at the Se sites (0.13 eV) than that at the Ni sites (0.87 eV). By creating Se-enriched 2D $NiSe_2$, the overpotential was further lowered to 117 mV at 10 mA cm^{-2} with a smaller Tafel slope of 32 mV dec^{-1}.[79] Similar high HER performance was also obtained from iron–nickel sulfide 2D materials synthesized by topotactic conversion.[77] Because H_2 prefers to form at the Fe sites rather than the Ni sites, Fe incorporation could change the catalytically active center and therefore facilitate the HER process. DFT simulations further confirmed the lower energy barrier for H^+ adsorption and higher exothermicity for H_2 formation on iron–nickel sulfide 2D materials when Fe was presented, which was believed to be the main reason for the improved HER performance.

In addition to material selection, point defects were often manipulated to further improve the catalytic performance of TMCs, including extrinsic dopant and intrinsic vacancy control. As discussed in Section 2.3, incorporating Mn ions in the $CoSe_2$ crystal lattice could induce subtle distortions in the atomic arrangement and consequently create additional exposed active edge sites. Moreover, the electronic structure of 2D $CoSe_2$ could be adjusted by Mn doping, which lowered the energy barriers of H–H bond formation and final H_2 release (Fig. 5g and h). As a result, Mn-doped 2D $CoSe_2$ displayed a much better HER catalytic activity than undoped $CoSe_2$, including lower overpotential of 174 mV, smaller Tafel slope of 36 mV dec^{-1}, and larger exchange current density of 68.3 μA cm^{-2}.[66] Vacancies, as a common intrinsic point defect, could also effectively modulate the HER performance of 2D materials. As an example, abundant sulfur vacancies confined in porous 2D Co_3S_4 were developed for HER catalysis.[80] The S-deficient 2D Co_3S_4 showed an extremely large mass activity of 1056.6 A g^{-1} at overpotential of 200 mV, which was superior to commercial Pt/C catalysts, and over 14 times and 107 times higher than the values for 2D Co_3S_4 and Co_3S_4 nanoparticles, respectively. Through electrochemical capacitance measurements, the amount of catalytically active sites was found to be significantly increased by the introduction of S vacancies into 2D Co_3S_4. DFT calculations revealed that Co_3S_4 with S vacancies had a larger adsorption energy toward H_2O molecules and relatively lower water-dissociation energy barrier, which could help reaching the intermediate catalyst-H stage and accelerate the kinetics for alkaline HER. Furthermore, the S vacancies could bring more electrons to the occupied states in the range from −0.26 eV to the Fermi level, affording enhanced electrical conductivity.

3.3. Metal nitrides

Metal nitrides are attractive for electrocatalytic HER mostly due to their metallic behavior, which can effectively facilitate electron transport during the HER process. Furthermore, the unique electronic structure of transition metal nitrides can provide suitable adsorption of H^+ on the crystal surfaces.[105] For example, Guo *et al.*[82] synthesized atomically thin metallic 2D Ni_3N by a simple annealing approach, which afforded excellent HER performance in the entire pH range (1–14) close to that of commercial Pt/C electrodes. It was found that Ni atoms accompanied by surrounding N atoms on the N–Ni surface acted as the most active HER sites (ΔG_H = 0.065 eV). Therefore, together with its good electrical conductivity, 2D Ni_3N exhibited excellent catalytic kinetics for HER as well as remarkable durability (negligible loss for over 5000 cycles). Furthermore, a holey structure has been introduced into 2D nitride materials to facilitate the diffusion of intermediates and gases during HER and to expose a larger number of catalytically active surface atoms in the hole area. Metallic 2D holey Ni_3Fe nitride (thickness: 0.6–0.8 nm) was synthesized by the nitridation treatment of the corresponding hydroxide precursors. They demonstrated excellent electrocatalytic performance for both HER and OER with a kinetic rate higher than that of the Pt/C catalyst.[106] However, due to the low valence state of the metal atoms, many metal nitrides oxidize during the electrocatalytic processes, which leads to relatively low stability. To resolve this problem, Jin *et al.* synthesized nitrogen-rich 2D metal nitrides (Mo_5N_6) with a higher Mo valence state, leading to better corrosion resistance toward HER.[83] Due to the incorporation of additional nitrogen atoms in the lattice, Mo_5N_6 showed a Pt-like electronic structure. As a result, Mo_5N_6 exhibited outstanding HER performance within the entire pH range. Furthermore, the HER activity with natural seawater showed highly stable catalytic current over 100 h, which outperformed commercial Pt/C and other metal nitride electrocatalysts. Nevertheless, although high HER performance has been demonstrated with 2D metal nitrides, their poor stability in aqueous electrolytes still largely limits their catalytic applications, particularly under high or low pH conditions.

3.4. Transition metal phosphides

In recent years, 2D nonlayered transition metal phosphides have emerged as another class of attractive electrocatalysts for HER due to their metalloid characteristics and good electrical conductivity. In particular, cobalt phosphide (CoP) has attracted widespread attention owing to their low cost, high catalytic activity, and optimal operational stability. Pu *et al.* developed a facile strategy to synthesize 2D CoP arrays on a Ti plate as a highly active HER catalyst *via* the low-temperature phosphidation of

α-$Co(OH)_2$/Ti precursor.[84] The CoP/Ti electrode showed higher HER activity in acidic solutions for low overpotential values of 90 and 146 mV at 10 and 100 mA cm^{-2}, respectively. Further, CoP/Ti afforded a Tafel slope of 43 mV dec^{-1} in the region of η = 40–120 mV. Furthermore, a CoP/Ti electrode exhibited good stability (10 000 s) and nearly 100% faradaic efficiency for H_2 evolution. Porous 2D CoP was also created with exposed reactive (200) facets *via* the phosphidation of Co_3O_4 precursors.[89] The as-synthesized 2D CoP showed outstanding HER performance in acidic solutions with even lower overpotential values of 56 and 131 mV at 10 and 100 mA cm^2, respectively; however, the Tafel slope (44 mV dec^{-1}) was almost the same as the solid 2D CoP discussed above. The stability was significantly improved to over 20 h. The extremely small thickness and porous structure rendered an extraordinarily high mass activity of 151 A g^{-1} at overpotential of 100 mV, which was ~80 times higher than that of CoP nanoparticles. To achieve the scalable application of 2D CoP electrocatalysts, Li *et al.* reported an ice-templating strategy to synthesize 2D CoP aerogels.[90] The highly porous aerogel structure afforded the advantages of short electron transfer distance and abundant exposed active sites, resulting in excellent electrocatalytic HER performance. The current density experienced a negligible loss at all pH values after 70 000 s, evidencing its remarkable stability. DFT calculations revealed that that P-top and Co bridge on the CoP(011) facet were the active sites for HER in acid and alkaline solutions, respectively (Fig. 6a and b). Because these active sites were always located on a defined crystal facet, single-crystal 2D structures could enable the exposure of the most active facets for HER. Li *et al.* presented the synthesis of various single-crystal 2D metal phosphides with well-defined exposed crystal facets by a salt-templating method. The as-synthesized 2D Co_2P with exposed (130) facets exhibited the greatest HER catalytic activity with overpotential of 41 mV at 10 mA cm^{-2} and Tafel slope of 35 mV dec^{-1} in 0.5 M H_2SO_4 solution as well as good stability.[91]

In addition to material selection, element doping could further improve the catalytic performance by tuning the electronic structure. Similar to TMC systems, Mo doping in 2D CoP induced a significant improvement in the HER activity with low overpotential values of 49 and 120 mV at 10 and 100 mA cm^{-2}, respectively.[93] Similar outstanding electrocatalytic HER activities were also demonstrated from a few other metal-doped 2D CoP materials (metal = Fe, Ni, and Mg).[88] Compared with the undoped one, Fe-doped 2D CoP exhibited superior HER activity with lower onset potential (~45 mV), overpotential of 188 mV at 100 mA cm^{-2}, and smaller Tafel slope of 76 mV dec^{-1}. XPS characterization revealed that the Co 2p and P 2p orbitals in Fe–CoP were positively and negatively shifted compared with those of pristine CoP (Fig. 6c and d), suggesting that Fe doping could enhance the electron interaction between Co and P. The adsorption behavior of H_2O on the electrocatalyst surface is an important factor for HER in a basic electrolyte. Theoretical study revealed that the electronic structure of Co was modulated by Fe incorporation (Fig. 6e and f), and the adsorption energy of the H_2O molecule on Fe–CoP (−0.05 eV) was much lower than that on CoP (−0.018 eV) (Fig. 6g), implying more thermodynamically favorable H_2O adsorption on Fe–CoP accounting for the largely enhanced HER activity.

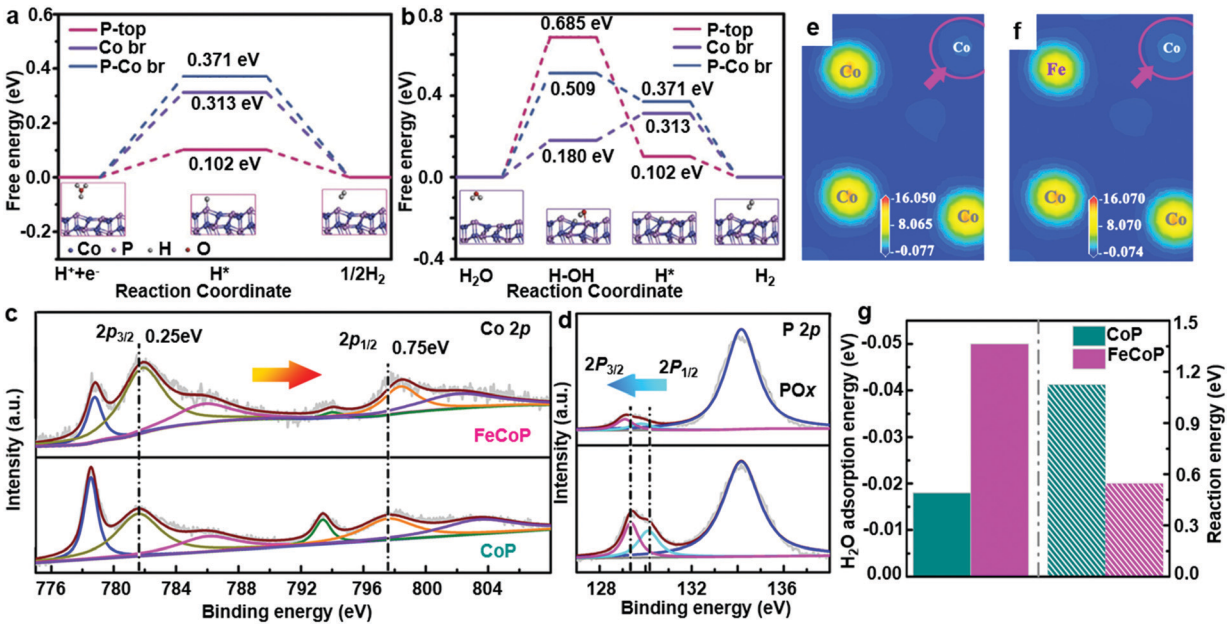

Fig. 6 2D transition metal phosphides for HER. (a) Corresponding free-energy diagram for HER of CoP(011) in the P-top, Co bridge, and P–Co bridge sites under the acidic condition. Top inset shows the simulated (011) facets of CoP. Co atoms: blue; P atoms: purple. (b) Corresponding free-energy diagram for the HER of CoP(011) for P-top, Co bridge, and P–Co bridge under the alkaline condition.[90] Reproduced with permission from © 2018 Wiley-VCH Verlag GmbH & Co. KGaA, Weinheim. XPS spectra of the (c) Co 2p and (d) P 2p orbitals of FeCoP; the charge density distributions of (e) FeCoP and (f) CoP; (g) adsorption energies of H_2O molecule and hydrogen-dissociation energy on the surface of CoP and FeCoP.[88] Reproduced with permission from © 2017 Elsevier Ltd.

In addition to CoP, other 2D transition metal phosphides also displayed comparable HER activities due to their similar crystal structures and electrochemical properties, which included NiP_2,[107] Ni_5P_4–Ni_2P,[85] MoP on carbon cloth,[87] porous Mo–W–P hybrids,[86] and phosphate-doped FeP.[92] Nevertheless, stability is also a major concern for these group of materials, because the surface reactions and reconstructions—particularly oxidation, reduction, and amorphization—can easily occur during the electrochemical processes.[108]

4. OER

In electrochemical water splitting, the efficiency is largely limited by the OER half reaction because of its sluggish reaction kinetics related to a complex four-electron redox process. During a typical OER process, H_2O first adsorbs at the active sites (*e.g.*, O vacancies) on the catalyst surface.[109] Upon receiving a hole, one H–O bond in the H_2O molecule is broken and oxidized to form OH*, which is further oxidized, affording O*. This O* then reacts with another H_2O molecule, forming OOH*, and eventually evolving into O_2 through a deprotonation process.[53] In this process, the active sites are essential in controlling the overall reaction rate. Increasing the number of active sites and improving their reactivity are two commonly used strategies to improve the OER electrocatalytic performance. Compared with other geometries, 2D nonlayered materials offer unique synergistic advantages for OERs, including large adsorption energy, fast electron transport, facile surface reaction, and easy electrolyte infiltration (Fig. 7a).[60,110]

DFT calculations that compared the catalytic activities of the (111) facets of monolayer and semibulk Co_3O_4 revealed the advantages of the 2D morphology.[111] Fig. 7b shows the OER pathway on the Co_3O_4(111) surface. The center chart shows the calculated reaction energies of each intermediate step for the two morphologies. According to the energy variations along the reaction pathways, the biggest difference lies in the adsorption of the second OH*, where the Co_3O_4 monolayer requires much less energy because the interaction between the two adsorbed OH* is much stronger. Furthermore, the following reaction steps on the monolayer also require less energy than those on the semibulk. Together, they result in a much lower overall OER energy barrier for the Co_3O_4 monolayer (3.85 eV) compared with that of the semibulk (4.31 eV). This calculation suggested that it is the structural distortion in the monolayer morphology that reduces the energy barrier and largely increases the activity of OER catalysis. Besides, similar to HER, the 2D nonlayered geometry also promotes oxygen reactivity by increasing the number of catalytically active sites and improving the electrical conductivity, owing to their extremely large number of unsaturated surface atoms and structural disorders associated with their atomic thickness. The doping of 2D lattices is also regarded as an effective strategy to improve the 2D conductivity and introduce more O vacancies that promote OER activity (Fig. 7c).[112,113] Nanoscale pores, which are often formed in solution-based synthesis processes, were found to facilitate catalysis as they promote electrolyte infiltration.

Further, 2D nonlayered materials always show superior OER activity over pure layered materials, owing to the extremely large number of unsaturated surface atoms and lattice distortion. For example, 2D nonlayered $CoSe_2$ is a promising candidate for achieving high OER performance with η_{10} of 0.32 V, while the performance of layered MoS_2 toward OER is limited under alkaline conditions. Layered double hydroxides (LDHs) are promising

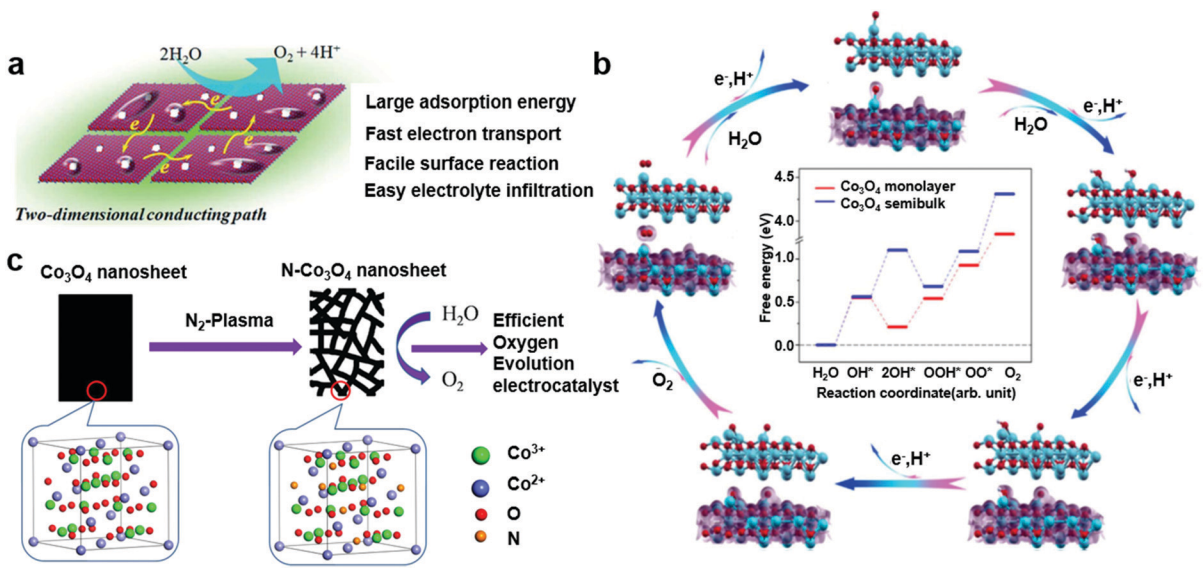

Fig. 7 Advantages of the 2D structure for OER. (a) 2D conducting path and advantages of atomically thin Co_3O_4 sheets for OER.[60] Reproduced with permission from © The Royal Society of Chemistry 2014. (b) DFT calculations on the screening of electrocatalytic activities on the (111) facets of Co_3O_4 monolayer and semibulk. Outer ring: schematic illustration of the OER process and valence-density isosurface for each reactant along the pathway. Center: the calculated free energies of the Co_3O_4 monolayer and semibulk.[111] Reproduced with permission from © 2016 Elsevier Ltd. (c) Schematic illustration of the preparation of N-doped 2D Co_3O_4 for efficient OER.[113] Reproduced with permission from © IOP Publishing Ltd. 2017.

candidates for OER because of their natural abundance and lower costs. However, the lack of active sites and poor electrical conductivity of LDHs make them unsuitable for electrocatalysis, and many efforts have been devoted in recent years toward increasing the active edge sites for higher OER performance. Pure-graphene- and g-C_3N_4-based layered materials have also shown poor intrinsic OER performance. It was found that spin redistribution induced by heteroatom doping in the graphene matrix can improve the OER catalytic activities. BP is another representative 2D layered material that has attracted increasing attention because of its lone pairs of electrons on the surface and its anisotropic electrical properties. However, similar to LDHs, the OER performance of bulk BP is also limited by insufficient active sites.

A summary of different 2D nonlayered materials and their characteristic parameters reported toward OER are listed in Table 2. Different from HER, 2D nonlayered OER catalysts are mostly oxides due to the requirement of H_2O adsorption. Our discussion will focus on these groups of materials and a few other alternatives that showed good H_2O adsorption capability.

4.1. Metal oxides

Metal oxides are the most commonly used OER catalysts due to their good stability and abundant O vacancies. In recent years,

Table 2 Summary of 2D nonlayered materials reported for OER electrocatalysts

Catalyst	Synthetic method (precursor)	Thickness	Electrolyte	Electrochemical performance	Ref., year
CoO	Ionic layer epitaxy method ($Co(NO_3)_2{\cdot}6H_2O$ and hexamethylenetetramine)	2.8 nm	1 M NaOH	Overpotential of 560 mV at 10 mA cm^{-2}; Tafel slope of ~85 mV dec^{-1} (*vs.* RHE)	53, 2017
Co_3O_4	Fast-heating strategy (CoO)	0.43 nm	1 M KOH	Electrocatalytic current of 341.7 mA cm^{-2} at 1.0 V *vs.* Ag/AgCl	60, 2014
Co_3O_4	One-step approach ($CoCl_2/K_3Co(CN)_6$)	1.5 nm	1 M KOH	Overpotential of 307 mV at 10 mA cm^{-2}; Tafel slope of 76 mV dec^{-1} (*vs.* RHE)	116, 2018
Co_3O_4	Self-assembly approach (polyethylene oxidepolypropylene oxide-polyethylene oxide)	1.8 nm	0.1 M KOH	Onset potential of 0.617 V *vs.* Hg/HgO; current density of 12.26 mA cm^{-2} at 0.8 V *vs.* Hg/HgO	111, 2016
Co_3O_4	Hydrothermal method ($NaBH_4$)	11 nm	1 M KOH	Overpotential of 318 mV at 10 mA cm^{-2} (*vs.* RHE); overpotential of 436 mV, the current density can be reached up to as high as 800 mA cm^{-2}	124, 2018
La_2O_3	Ionic layer epitaxy method ($La(NO_3)_3$, hexamethylenetetramine, oleylamine)	2.27 nm	1 M NaOH	Overpotential of 310 mV at 10 mA cm^{-2}; Tafel slope of 43.1 mV dec^{-1} (*vs.* RHE)	46, 2019
N-Doped Co_3O_4	N_2 plasma (Co_3O_4)	—	0.1 M KOH	Overpotential of 310 mV at 10 mA cm^{-2}; Tafel slope of 59 mV dec^{-1} (*vs.* RHE)	113, 2017
CuO	Chemical bath deposition method ($CuSO_4$, NH_4OH)	10–15 nm	1 M KOH	Overpotential of 350 mV at 10 mA cm^{-2}; Tafel slope of 59 mV dec^{-1} (*vs.* RHE)	110, 2017
NiTi oxide	Reverse microemulsion method (TiO_2, NiTi-LDH)	1 nm	1 M KOH	Overpotential of 320 mV at 10 mA cm^{-2}; Tafel slope of 52 mV dec^{-1} (*vs.* RHE)	109, 2016
$NiCo_2O_4$	Topochemical method (NiCo hydroxies)	1.56 nm	1 M KOH	Current density of 285 mA cm^{-2} at 0.8 V (*vs.* RHE); overpotential of 0.32 V (*vs.* RHE)	115, 2015
Fe_1Co_1-oxide	Solution reduction method ($Fe(NO_3)_3$, $Co(NO_3)_2$, CTAB)	1.2 nm	0.1 M KOH	Overpotential of 308 mV at 10 mA cm^{-2}; Tafel slope of 36.8 mV dec^{-1} (*vs.* RHE)	125, 2017
$Fe_1Co_1O_x$	Hydrothermal and hydrogenation method ($Fe(NO_3)_3$, $Co(NO_3)_2$, and CTAB)	1.2 nm	1 M KOH	Overpotential of 225 mV at 10 mA cm^{-2}; Tafel slope of 36 mV dec^{-1} (*vs.* RHE)	126, 2018
Co_3S_4	Ultrasound exfoliation treatment Co_3S_4/triethylenetetramine	1.0 nm	Neutral solution	Overpotential of 0.7 V at 3.97 mA cm^{-2}; overpotential at 0.31 V (*vs.* RHE)	121, 2015
Co_9S_8	Polyol refluxing, sulfurization and calcination process (graphene oxides or $Co(Ac)_2$)	3–4 nm	1 M KOH	Overpotential of 266 mV at 10 mA cm^{-2}; Tafel slope of 75.5 mV dec^{-1} (*vs.* RHE)	119, 2019
Co_9S_8	Microwave-assisted liquid-phase growth ($Co(OH)_2$)	0.98 nm	1 M KOH	Overpotential of 288 mV at 10 mA cm^{-2} (*vs.* RHE)	120, 2018
$CuCo_2S_4$	Metal activity and structure-directed one-pot sulfurization strategy (Cu and Co ions)	10–13 nm	0.1 M KOH	Overpotential of 337 mV at 10 mA cm^{-2} (*vs.* RHE)	122, 2016
FeS_2/CoS_2	Sulfurization and calcination method ($CoFe_2O_4$)	1.6–2.8 nm	1 M KOH	Overpotential of 302 mV at 100 mA cm^{-2}; Tafel slope of 42 mV dec^{-1} (*vs.* RHE)	123, 2018
Co-Based MOFs	Surfactant-assisted hydrothermal method (Co^{2+} and benzenedicarboxylic acid (BDC))	2 nm	1 M KOH	Overpotential of 263 mV at 10 mA cm^{-2}; Tafel slope of 74 mV dec^{-1} (*vs.* RHE)	127, 2018
NiCo bimetal-MOFs	Ultrasonic method (Ni^{2+}, Co^{2+} and BDC)	3.1 nm	1 M KOH	Overpotential of 189 mV at 10 mA cm^{-2}; onset potential of 1.39 V (*vs.* RHE)	128, 2016
CoCo LDH[a]	Exfoliation method	1 layer	1 M KOH	Overpotential of 319 mV at 10 mA cm^{-2}; Tafel slope of 42 mV dec^{-1} (*vs.* RHE)	129, 2019
MoS_2[a]	Chemical stripping	1.5 nm	0.5 M H_2SO_4	Overpotential of 450 mV at 10 mA cm^{-2}; Tafel slope of 322 mV dec^{-1} (*vs.* RHE)	130, 2016
g-C_3N_4[a]	Ultrasonic exfoliation	1.1 nm	0.1 M KOH	Overpotential of 734 mV at 7.1 mA cm^{-2}; Tafel slope of 120.9 mV dec^{-1} (*vs.* RHE)	131, 2014
Graphene[a]	*In situ* dissection	5–7 layer	1 M KOH	Overpotential of 1.8 V at 20.95 mA cm^{-2}; Tafel slope of 43.1 mV dec^{-1} (*vs.* RHE)	132, 2017
Black Phosphorus[a]	Solution-phase exfoliation	6 nm	1 M KOH	Onset-potential 145 mV; Tafel slope of 88 mV dec^{-1} (*vs.* RHE)	133, 2017

[a] Representative 2D layered materials for comparison.

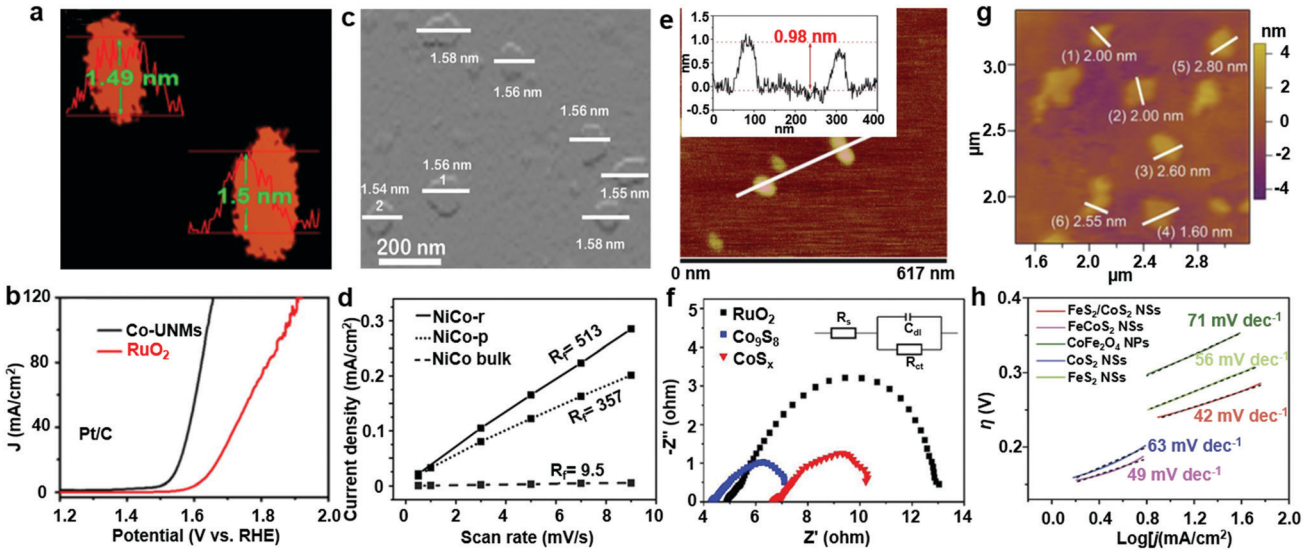

Fig. 8 Different types of 2D nonlayered materials for OER. (a) AFM image of 2D Co_3O_4 with the corresponding height profiles. (b) The iR-corrected LSV curves of 2D Co_3O_4 and commercial RuO_2 in O_2-saturated 1 M KOH electrolyte at a scan rate of 5 mV s^{-1}.[116] Reproduced with permission from © 2018 American Chemical Society. (c) AFM image and height profiles of 2D $NiCo_2O_4$. (d) R_f values of 2D $NiCo_2O_4$ with rich oxygen vacancies (NiCo-r) and poor oxygen vacancies (NiCo-p), as well as a bulk sample; the measurements were performed at 0.24 V in 1 M KOH solution at scan rates from 0.5 to 9 mV s^{-1} of the corresponding CVs.[115] Reproduced with permission from © 2015 Wiley-VCH Verlag GmbH & Co. KGaA, Weinheim. (e) AFM image and height profiles of 2D CoS_x. (f) Nyquist plots of 2D CoS_x and Co_9S_8 (annealed CoS_x), and commercial RuO_2 in the frequency range from 100 kHz to 0.01 Hz for η = 365 mV.[120] Reproduced with permission from © The Royal Society of Chemistry 2018. (g) AFM image of 2D FeS_2/CoS_2 with the corresponding height profiles. (h) Tafel plots of different catalysts at the scan rate of 2 mV s^{-1} in 1 M KOH electrolyte.[123] Reproduced with permission from © 2018 Wiley-VCH Verlag GmbH & Co. KGaA, Weinheim.

many earth-rich transition metal oxides (TMOs) like CoO,[53] Co_3O_4,[111] CuO,[110] NiO,[109,114] La_2O_3,[46] and $NiCo_2O_4$[115] have been extensively studied as OER catalysts to replace noble metal oxides such as RuO_2 and IrO_2. Among them, Co_3O_4 distinguishes itself due to its high performance and good sustainability (*e.g.*, environment-friendliness and rich reserves). Li *et al.* synthesized 2D Co_3O_4 through a facile and scalable surfactant-free cyanogel–$NaBH_4$ method.[116] Further, 2D Co_3O_4 exhibited a uniform thickness of ~1.5 nm and was rich with nanoscale pores (Fig. 8a). The pores were formed during the assembly of crystal nuclei. As shown in Fig. 8b, when applied to OER, 2D Co_3O_4 showed onset potential of 101 mV, which was lower than that of commercial RuO_2 (408 mV). The overpotential of 2D Co_3O_4 at a current density of 10 mA cm^{-2} was also ~100 mV lower than that of RuO_2. This performance enhancement could be attributed to the high surface area and abundant defect sites at the pore edges, thereby favoring mass transport.

To improve the O-vacancy concentration, Bao *et al.* created bimetallic oxide ($NiCo_2O_4$) with the 2D morphology (Fig. 8c).[115] The as-prepared 2D $NiCo_2O_4$ had a thickness of 1.6 nm (two unit cells). Rich O vacancies were induced as a result of calcination in an oxygen-deficient atmosphere, which improved the reactivity of active sites and reduced the H_2O adsorption energy. This ultrathin thickness improved the amount of active sites and therefore facilitated the surface reactions. The roughness factor (R_f) calculated from the cyclic voltammetry data of 2D $NiCo_2O_4$ with rich O vacancies (NiCo-r) and poor O vacancies (NiCo-p) were both 40–50 times larger than that of the bulk sample (Fig. 8d). The higher R_f value represented more surface active sites, confirming the advantage of 2D morphology for enhancing the electrocatalytic performance.

4.2. TMCs

In addition to the capability of serving as descending HER catalysis, some TMCs also acted very effectively in OER processes. Nevertheless, the fundamental mechanism of TMCs for OER has not been fully understood yet.[117,118] It was suggested that TMCs could be oxidized into the corresponding metal oxides/hydroxides on the surface in strongly oxidative environments of OER. The fresh surfaces were usually more catalytically active compared with metal oxides/hydroxides that were synthesized directly. Therefore, TMCs like Co_3S_4, Co_9S_8, and $CuCo_2S_4$ represent a unique group of materials that can be used for catalyzing fully electrocatalytic water-splitting reactions.[119–122] In a representative example, 2D CoS_x synthesized by post-sulfurizing $Co(OH)_2$ were used for OER, HER, and overall water splitting.[120] The as-synthesized 2D materials had a thickness of less than 1 nm and size of ~100 nm (Fig. 8e). The large number of exposed surface atoms contributed to the high electrocatalytic activity, and the ultrathin and mesoporous structures facilitated mass and charge transfer through the 2D structure. The Nyquist plots from the electrochemical impedance spectroscopy (EIS) data revealed that the charge transfer resistances of 2D CoS_x and Co_9S_8 (annealed CoS_x) were much lower than that of commercial RuO_2 (Fig. 8f). It revealed the faster faradaic process and higher electric conductivity at the electrode–electrolyte interface of 2D CoS_x and Co_9S_8. Further, 2D FeS_2/CoS_2 mixture with thicknesses from 1.6 to 2.8 nm were prepared by annealing $CoFe_2O_4$ nanoparticles with

sublimed sulfur in a N_2 atmosphere (Fig. 8g).[123] As shown in Fig. 8h, the Tafel slope of 2D FeS_2/CoS_2 (42 mV dec^{-1}) was lower than those for $CoFe_2O_4$ nanoparticles and other catalysts, demonstrating a higher OER reaction rate. The superb OER performance could be attributed to the large specific surface area of the 2D structure and rich interface defects that facilitate the adsorption and activation of the reactants. The superior catalytic performance for both OER and HER suggested that 2D TMCs may hold a unique advantage for commercial overall water-splitting applications.

4.3. MOFs

MOFs are composed of coordination bonds between the metal-atom nodes and organic ligands with periodic structural units. Owing to their active transition metal centers and uniform porous structure, MOFs are promising as electrocatalysts for OERs. Nevertheless, thin-film electrodes built on MOFs suffer from low conductivity, poor mass permeability, and blockage of active metal centers by organic ligands, which greatly limit their applications in electrocatalysis. Thinning MOFs to 2D morphology has been considered to be an effective way to achieve high-performance MOFs-based OER electrocatalysts.[127,128] The electron transfer and mass transport properties could be largely improved by the 2D MOF structure. In addition, the rich, coordinatively unsaturated metal sites are favorable for adsorption and are the dominating active centers for OER.[128] Zhao *et al.* developed 2D NiCo MOFs through a simple ultrasound method for OER electrocatalysis.[128] In O_2-saturated 1 M KOH solution at a scan rate of 5 mV, the 3.1 nm-thick NiCo MOF exhibited much lower overpotential of 250 mV at 10 mA cm^{-2} compared with bulky NiCo MOF nanosheets (317 mV), Co MOF nanosheets (371 mV), Ni MOF nanosheets (321 mV), and commercial RuO_2 (279 mV). In addition to the large quantity of exposed coordinatively unsaturated surface metal atoms, the coupling effect between Co and Ni also had a favorable contribution to the OER enhancement. The XPS results revealed that a part of the electrons are transferred from Ni^{2+} to Co^{2+} through the oxygen of the ligands. Such a coupling effect between Ni and Co could induce a change in the e_g-orbital filling and improve their OER performance.[134] The 2D NiCo MOFs provided a promising alternative for heterogeneous electrocatalysts toward OER under alkaline conditions.

5. ORR

ORR is a critical reaction in fuel cells and metal–air batteries, where oxygen is reduced to O^{2-} upon the receipt of electrons. The ORR mechanism is complex and includes a multistep electron transfer process.[135–137] As shown in Fig. 9a, the reaction may go through two different pathways in an aqueous solution. One pathway is a four-electron ($4e^-$) process, where O_2 is directly reduced to H_2O (in acid electrolytes) or OH^- (in alkaline electrolytes). The other one includes two successive two-electron ($2e^-$) processes, which involves the production of peroxide intermediates (in acid electrolytes) or HO_2^- intermediates (in alkaline electrolytes) from O_2.[30] In an ORR process, hydrogen can react with the oxygen either on the surface *via* the Langmuir–Hinshelwood (LH) mechanism or in the electrolyte *via* the Eley–Rideal (ER) mechanism, depending on the reaction conditions.[138] The energy plots shown in Fig. 9b reveal that both classes of reactions (LH and ER) possibly occur at electrode potentials near 1.23 eV, and the corresponding reduction potential of the ORR was calculated by the Nernst equation. Individual ER reaction barriers are lower than the LH barriers at the ideal calculated potential of 0 V. With the applied electrode potential, the barrier heights of escaping the bound O* and OH* intermediates can be changed, as shown in Fig. 9c.

Recently, 2D nonlayered materials have shown promising application potential in ORR electrocatalysis. The 2D-morphology-related advantages, such as a large number of surface active sites, enhanced

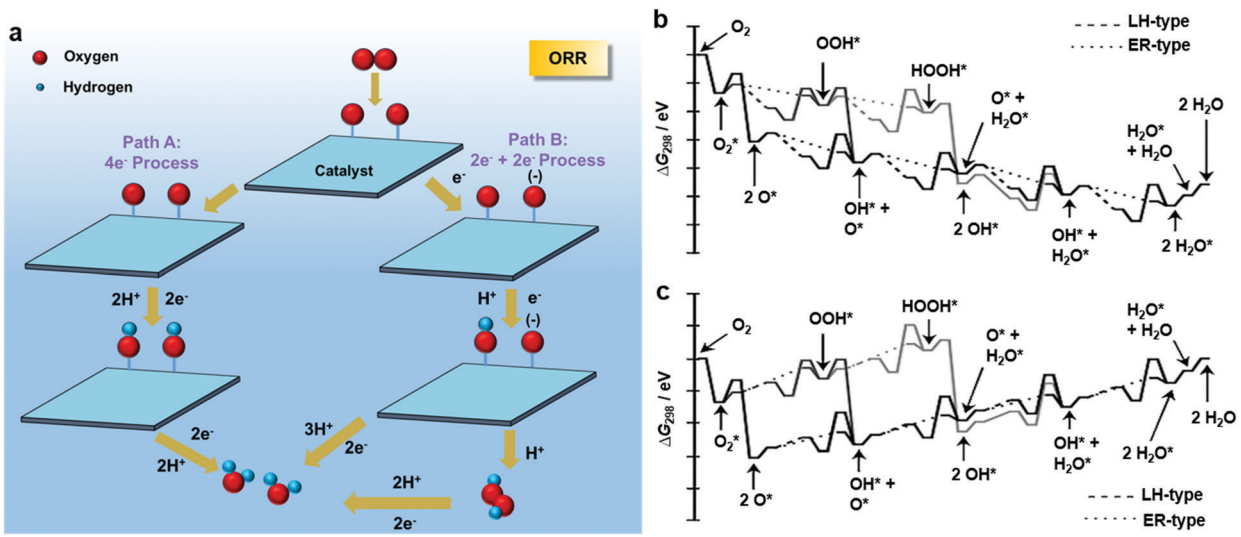

Fig. 9 Mechanism of ORR. (a) Schematic diagram of the ORR mechanism in aqueous media.[137] Reproduced with permission from © 1997 Elsevier Ltd. The energy plots of LH and ER reaction mechanisms for ORR (b) at the ideal calculated potential of U = 0 V, (c) U = 1.14 eV (*vs.* RHE).[138] Reproduced with permission from © 2010 Wiley-VCH Verlag GmbH& Co. KGaA, Weinheim.

Table 3 Summary of 2D nonlayered materials reported for ORR electrocatalysts

Catalyst	Synthetic method (precursor)	Thickness	Electrolyte	Electrochemical performance	Ref., year
Core–shell $Pd@Pt_{monolayer}$	Defect-mediated thin film growth method	4.7 nm	0.1 M $HClO_4$	Half-wave potential of 0.874 V; mass activity (A_m): 0.717 A mg^{-1} at 0.9 V (*vs.* RHE)	142, 2015
PtPd alloy	Fast one-pot aqueous method (metal $PtCl_6^{2-}$ and $PdCl_4^{2-}$)	6.0 nm	0.1 M KOH	Half-wave potential of 0.879 V; mass activity: 382.10 mA mg^{-1} at 0.80 V (*vs.* RHE)	144, 2019
$Pt_{32}Pd_{48}Ni_{20}$	A robust and general wetchemical route ($Pt(acac)_2$, $Pd(acac)_2$, $Ni(acac)_2$, $Mo(CO)_6$)	1.4 nm	0.1 M KOH	Mass activities: 0.54 A mg^{-1} at 0.9 V (*vs.* RHE)	148, 2019
$NiCo_2O_4$	Thermal treatment (Zn–Co hydroxide)	2.4 nm	0.1 M KOH	Onset potential of 0.85 V and half-wave potential of 0.74 V; Tafel slope of 68 mV dec^{-1} (*vs.* RHE)	145, 2019
$ZnCo_2O_4$	Thermal treatment (Zn–Co-LDH)	Ultrathin	0.1 M KOH	Average electron transfer number (n): 4.1 (*vs.* RHE)	146, 2018
$CuCo_2S_4$	One-pot sulfurization ($Cu(acac)_2$, $Co(acac)_2$ dodecylamine, DDT)	10–13 nm	0.1 M KOH	Onset potential of 0.90 V; half-wave potential of 0.74 V; Tafel slope: 74 mV dec^{-1} (*vs.* RHE)	122, 2016
$FeNiS_2$	A facile colloidal method ($Fe(acac)_3$, $Ni(aca)_2$, OTT, OAM, ODE)	2–3 nm	0.1 M KOH	Onset potential of 0.78 V; current density: 3.2 mA cm^{-2} at 0.45 V; Tafel slope: 107 mV dec^{-1} (*vs.* RHE)	149, 2016
Pt embedded MOFs	Ultrasonication-assisted wet chemical method	2–4 nm	0.1 M KOH	Half-wave potentials of 75 mV (Co as the metal nodes); half-wave potentials of 48 mV (Ni as the metal nodes); electrons transferred: 4 (*vs.* RHE)	150, 2018

charge/mass transport, and extensive contact area with the electrolyte play an important role in boosting the ORR performance. Although ORR requires the supply of electrons for HER, the surface needs to have strong affinity toward oxygen species. Therefore, a number of 2D nonlayered electrocatalysts have been developed for ORR from metal oxides, metals, and MTCs, as they are good electronic conductors and possess low oxygen adsorption energies, which are favorable for the adsorption and reaction of oxygen on their surfaces. A summary of 2D nonlayered electrocatalysts for ORR is shown in Table 3.

5.1. Metals

In proton-exchange-membrane (PEM) fuel cells, the cathode usually requires a large amount of Pt to catalyze the sluggish ORR.[139–141] In order to reduce the use of the noble metal Pt and reduce costs, it is important to improve its utilization. Here, 2D morphology is a promising strategy to maximize the specific surface area with the desired catalytic activity and durability. Wang *et al.* synthesized 2D core–shell $Pd@Pt_{monolayer}$ on a Pd substrate that showed excellent electrocatalytic activity and stability for ORR in acidic electrolytes.[142] The use of Pd substrates was found to improve the ORR activity, because it could reduce the surface oxygen affinity of Pt. Atomically smooth Pt skin was synthesized by defect-mediated membrane growth followed by the formation of Pd coating. The 2D $Pd@Pt_{monolayer}$ had a thickness of $\sim$4.7 nm (Fig. 10a), and it exhibited enhanced kinetic activities across the entire potential region compared with commercial Pt/C (Fig. 10b). The area-specific activity (A_s) of 2D $Pd@Pt_{monolayer}$ reached 0.438 A cm^{-2} at 0.9 V, and its corresponding mass activity (A_m) was 0.717 A mg^{-1}. These A_s and A_m values were 3.4 and 6.6 times higher than those of the commercial Pt/C catalyst (A_s = 0.128 A cm^{-2}; A_m = 0.109 A mg^{-1}), respectively, and reached the US DOE 2017 target for Pt-based ORR catalysts (A_m = 0.44 A mg^{-1}).[143] Further, 2D materials from bimetallic Pt/Pd alloy were also reported for ORR and similarly higher electrocatalytic activity was obtained compared with commercial Pt/C catalysts.[144]

5.2. Metal oxides

Due to their oxygen affinity and abundance, metal oxides are a natural choice as ORR electrocatalysts. Among them, complex metal oxides such as $NiCo_2O_4$ and $ZnCo_2O_4$ have often afforded higher activity toward ORR when compared with binary metal oxides.[145,146] These oxides usually have a spinel structure, where the different octahedral metal ions in the spinel could facilitate the activation and cleavage of O–O bonds and therefore facilitate ORR.[147] However, the activity of spinel oxides for ORR is still insufficient for practical applications, such as Zn–air batteries. Improving their catalytic performance for ORR remains a critical challenge. Liu *et al.* synthesized 2 nm-thick 2D $NiCo_2O_4$ for ORR (Fig. 10c).[145] Owing to its ultrathin features and higher concentration of O vacancies formed by oxygen-deficient calcination, 2D $NiCo_2O_4$ exhibited improved electrocatalytic performance toward ORR at onset potential of 0.85 V. Zn–air batteries assembled from 2D $NiCo_2O_4$ showed a comparable performance as commercial Pt/C. As shown in Fig. 10d, 2D $NiCo_2O_4$ materials calcined in air, O_2, and H_2/Ar are denoted as NiCo–air, NiCo–O_2, and NiCo–H_2/Ar, respectively. The electron transfer numbers of NiCo–H_2/Ar, NiCo–O_2, NiCo–air, and Pt/C were 3.80, 3.90, 3.94, and 3.99, respectively, which confirmed that the ORR processes mainly consisted of four-electron reduction; further, the performance of NiCo–air was very close to that of commercial Pt/C catalysts. Meanwhile, the HO_2^- yields of 2D NiCo–air were also close to those of commercial Pt/C. Zn–air batteries assembled from 2D $NiCo_2O_4$ showed a smaller discharging/charging voltage gap and higher stability compared with commercial Pt/C. The 2D structure significantly increased the number of active sites at these spinel oxides, showing good promise toward replacing noble metal catalysts in ORR, such as Zn–air battery applications.

5.3. TMCs

Since Cu^-- and Co^--based nanocrystals have been considered to be good electrocatalysts for ORR, 2D TMCs of the relevant compounds, such as $CuCo_2S_4$ and $FeNiS_2$, have also been studied for ORR applications.[122,149] Wang *et al.* adopted a

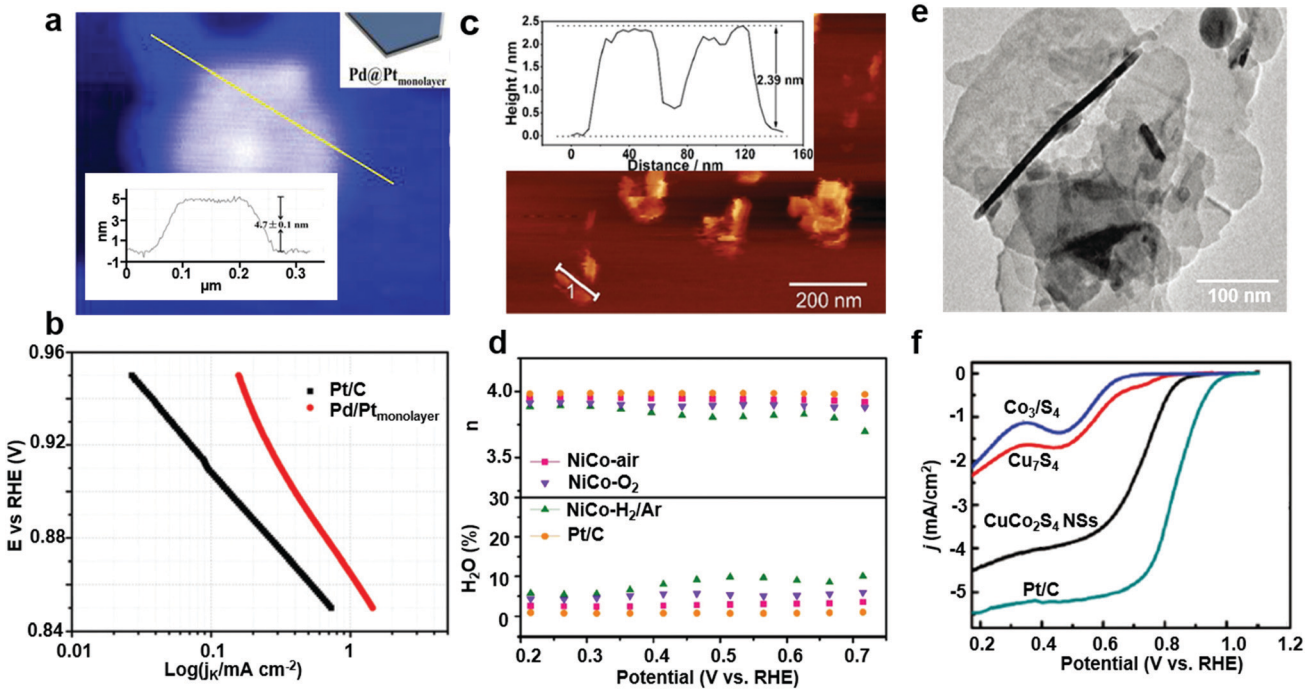

Fig. 10 Different types of 2D nonlayered materials for ORR. (a) AFM images of the core–shell-structured 2D $Pd@Pt_{monolayer}$ and the corresponding height details along the yellow line. (b) Area-specific kinetic current densities (j_K) of 2D $Pd@Pt_{monolayer}$ and commercial Pt/C in O_2-purged 0.1 M $HClO_4$ solution.[142] Reproduced with permission from © 2013 The Royal Society of Chemistry. (c) AFM image of the as-prepared 2D $NiCo_2O_4$ calcined in air and the corresponding height profile. (d) Electron transfer number and percentage of peroxides with respect to the total oxygen reduction products for 2D $NiCo_2O_4$ calcined in air, O_2, H_2/Ar, and Pt/C electrode in O_2-saturated 0.1 M KOH solution.[145] Reproduced with permission from © 2019 Elsevier B.V. (e) TEM image of 2D $CuCo_2S_4$. (f) ORR polarization plots of 2D $CuCo_2S_4$, Cu_7S_4 nanodisks, Co_3S_4 nanocrystals, and Pt/C catalysts in O_2-saturated 0.1 M KOH solution at a rotation rate of 1600 rpm.[122] Reproduced with permission from © 2016 The Royal Society of Chemistry.

"leveling metal activity and structure-directed one-pot sulfurization" strategy to prepare 2D $CuCo_2S_4$, which mainly exposed their (111), (022), and (004) facets.[122] The as-synthesized 2D $CuCo_2S_4$ had a circular sheet-like structure with a diameter of ~100–200 nm (Fig. 10e). The LSV curve of 2D $CuCo_2S_4$ was compared to three other control catalysts with respect to ORR on a rotating disk electrode at a rotation speed of 1600 rpm in O_2^--saturated 0.1 M KOH aqueous solution (Fig. 10f). The half-wave potential and onset potential of 2D $CuCo_2S_4$ were 0.74 and 0.90 V (*vs.* RHE), respectively. These values were higher than those of metal chalcogenides, such as Cu_7S_4 nanodisks, Co_3S_4 nanocrystals, and other reported ORR catalysts (*e.g.*, Pd-$H_3PW_{12}O_4$-CMK_3, defective TiO_2, and delithiated $Li_{1-x}CoO_2$).[151–153] Although this ORR electrocatalytic activity was still slightly lower than that of commercial Pt/C, the creation of the 2D morphology already demonstrated strong potential toward the use of earth-abundant materials to replace precious-metal-based catalysts. The enhanced activity of 2D $CuCo_2S_4$ could be attributed to the component effect and efficient electronic coupling between the two metal cations with different oxidation states (+1 for Cu, +2.4 for Co), as well as its ultrathin 2D geometry. Similar enhancements were observed from other 2D nonlayered TMCs such as $FeNiS_2$.[149] Here, 2D $FeNiS_2$ also exhibited superior ORR electrocatalytic activity over those of Ni_9S_8 nanorods and 2D FeS under the same conditions, as well as long-term stability, suggesting they may be useful as practical noble-metal-free electrocatalysts.

6. Electrocatalytic CO_2 reduction

The electroreduction of CO_2 with well-defined catalysts is a promising strategy to reduce the greenhouse effect and produce value-added products. Electroreduction is attractive due to the environmental compatibility coupling with carbon-free renewable energy sources such as solar, tidal, and wind.[154] Typically, the electrochemical reduction of CO_2 at the electrode–electrolyte interfaces comprises three major steps: (i) the chemical adsorption of CO_2 on the surface of an electrocatalyst (cathode); (ii) electron transfer and/or proton migration to dissociate C═O bonds and/or to form C–H bonds; and (iii) the desorption of products from the catalyst surface. In CO_2 electroreduction, the crucial step is CO_2 activation, which involves one-electron transfer to form a radical anion ($CO_2^{\bullet-}$). However, CO_2 is chemically inert, which has low electron affinity and very large energy gap (13.7 eV) between its lowest unoccupied molecular orbital and highest occupied molecular orbital. The activation of CO_2 into the radical anion ($CO_2^{\bullet-}$) is thermodynamically unfavorable, which requires high reduction potential of −1.9 V *vs.* SHE.[155]

After the formation of $CO_2^{\bullet-}$ radicals, several proton-assisted multielectron transfer reactions can take place more efficiently, as these reactions are at lower energy costs compared with the first activation step. Based on the number of electrons and protons transferred, CO_2 can be reduced to different products,

Table 4 Summary of 2D nonlayered materials reported for CO_2 reduction electrocatalysts

Catalysts	Synthetic method (precursor)	Thickness	Electrolytes	Current density	Overpotential	Products (FE)	Ref., year
Ag nanoplate	Chemical reduction ($AgNO_3$)	—	0.1 M $KHCO_3$	1.2 mA cm^{-2} @ −0.856 V (*vs.* RHE)	η: 0.45 V @ 1.2 mA cm^{-2}	CO: 96.8% @ −0.855 V (*vs.* RHE)	162, 2017
Ag	Electrochemical oxidative–reductive approach	~50 nm	0.5 M $NaHCO_3$	10 mA cm^{-2}@ −0.8 V (*vs.* RHE)	η: 0.29 V @ 5 mA cm^{-2}	CO: 95% @ −0.7 V (*vs.* RHE)	159, 2017
Pd	CO-assisted method ($Pt(acac)_2$ DMF, PVP)	5 atomic thickness	0.1 M $KHCO_3$ solution	14 mA cm^{-2} @ −0.9 V (*vs.* RHE)	Onset potential: −0.2 V (*vs.* RHE)	CO: 94% @ −0.5 V (*vs.* RHE)	161, 2018
Sn sheets confined in graphene	Spatially confined reduction strategy (SnO_2)	1.4 nm	0.1 M $NaHCO_3$	21.1 mA cm^{-2} @ −1.8 V (*vs.* SCE)	Onset potential: −0.85 V (*vs.* SCE)	$HCOO^-$: 89% @ −1.8 V (*vs.* SCE)	163, 2016
Co_3O_4	Fast-heating ($Co(CO_3)_{0.5}(OH)\cdot 0.11H_2O$)	1.72 nm	0.1 M $KHCO_3$	0.68 mA cm^{-2} @ −0.88 V (*vs.* SCE)	Onset potential: −0.82 V (*vs.* SCE)	$HCOO^-$: 64.3% @ −0.88 V (*vs.* SCE)	166, 2016
Oxygen-deficient Co_3O_4	Fast-heating process ($Co(CO_3)_{0.5}(OH)\cdot 0.11H_2O$)	0.84 nm	0.1 M $KHCO_3$	2.7 mA cm^{-2} @ −0.87 V (*vs.* SCE)	Onset potential: −0.78 V (*vs.* SCE)	$HCOO^-$: 87.6% @ −0.87 V (*vs.* SCE)	167, 2017
Mesoporous SnO_2	Calcination in air (2D SnS_2)	<10 nm	0.5 M $NaHCO_3$	50 mA cm^{-2} @ −1.6 V (*vs.* Ag/AgCl)	η: 0.88 V @ 45 mA cm^{-2}	$HCOO^-$: 89% @ −1.6 V (*vs.* Ag/AgCl)	168, 2017

such as CO, formic acid (HCOOH), formaldehyde (HCHO), methanol (CH_3OH), methane (CH_4), ethylene (C_2H_4), ethanol (C_2H_5OH), and ethane (C_2H_6). A big challenge for electroreduction is the lack of product selectivity due to the high activity of $CO_2^{\bullet-}$ radicals, small potential differences among the various products, and competitive side reactions, *e.g.*, HER leading to the formation of H_2. Another concern is the stability of the electrocatalyst due to the deactivation by reaction intermediates and byproducts. Due to the large number of low-coordinated surface atoms, 2D nonlayered materials have recently attracted considerable attention for electrocatalytic CO_2 reduction. A summary of 2D nonlayered electrocatalysts reported for CO_2 reduction is shown in Table 4. Further, 2D nonlayered materials exhibit controllable electronic structures, high active site density, enhanced charge mobility, suitable binding affinity to carbon dioxide, and/or reaction intermediates. These attractive properties lead to the fabrication of promising electrocatalysts with unique activity, selectivity, and stability.

6.1. Metals

Various metallic electrocatalysts such as Au, Pd, Ag, and Zn have been studied for CO_2 reduction.[156–160] The surface of these metals can weakly bind CO and exhibit relatively high CO_2 reduction efficiencies to CO rather than competitive H_2 derived from HER. Here, 2D metals with a substantial number of exposed active sites appeared to be beneficial for fast interfacial charge transfer and facile electrochemical catalysis. Recently, Zhu *et al.* observed that 2D Pd could effectively reduce the onset potential for CO formation by exposing abundant atoms with a relatively low coordination number.[161] The as-synthesized 2D Pd was rather small, ranging from ~5 to 50 nm (Fig. 11a). Further, 2D materials with a thickness of five atomic layers and 5.1 nm edge length reached the CO faradaic efficiency of 94% at −0.5 V, which appeared to be the most efficient among all the Pd-based catalysts for CO_2 electroreduction (Fig. 11b). Compared with similar-sized Pd nanoparticles, 5.1 nm 2D Pd showed over five times greater mass activity of 140 A g^{-1} at −0.9 V. DFT calculations further demonstrated that the enhanced catalytic activity originated from more exposed atoms with an average coordination number of around 5 (Fig. 11c).

Crystal facets also play a significant role in determining the reaction activity and selectivity. Different surface facets show different Lewis acidity and polarizing power, thereby influencing CO_2 adsorption and activation. Predominant shape-dependent electrocatalytic reduction of CO_2 to CO on 2D triangular silver nanoplates was demonstrated.[162] Triangular Ag nanoplates enclosed by the (100) and (111) facets were synthesized through a wet-chemical approach. For CO_2 reduction reaction, this 2D Ag exhibited higher Faraday efficiency (96.8%) for CO formation at fixed potential of −0.855 V (*vs.* RHE) as compared to similarly sized Ag nanoparticles and bulk Ag (Fig. 11d). DFT calculations indicated that the high selectivity of CO at ultralow overpotential stemmed from the combination of the predominant exposure of the (100) facets (Fig. 11e) and the optimum edge-to-corner ratio (Fig. 11f).

Although 2D metals with a very large amount of exposed surface atoms can be highly active CO_2 electroreduction catalysts, some of them tend to be very unstable at ambient conditions and can be oxidized in an uncontrolled manner, which can lead to the loss of electronic conductivity and stability. Further, 2D hybridization could avoid the oxidation of highly reactive metals and improve the catalytic activity. Lei *et al.* reported highly reactive Sn quantum sheets confined in graphene showed enhanced electrocatalytic activity and stability.[163] Further, 2D Sn with lowered coordination numbers confined in graphene can efficiently stabilize the carbon dioxide radical anion.

In addition to increasing the stability, 2D hybridization could also promote selectivity toward CO_2 electroreduction. Dai *et al.* developed a simple strategy to prepare air-stable 2D $Cu/Ni(OH)_2$. With stable exposure of the Cu(111) facets, the hybrids exhibited high activity and selectivity for the reduction of CO_2 to CO, delivering a current density of 4.3 mA cm^{-2} at low overpotential of 0.39 V with high faradaic efficiency (92%). Moreover, there was no obvious decay in the catalytic performance for over 22 h, indicating excellent stability for the electroreduction of CO_2.[164] It has also been found that 2D hybridization could modify the binding strength of the catalytic products on metal surfaces and therefore change the catalytic activities. Zhang *et al.* prepared 2D Pd partially capped by SnO_2 nanoparticles. Such structural design not only enhanced the adsorption of CO_2 on SnO_2, but

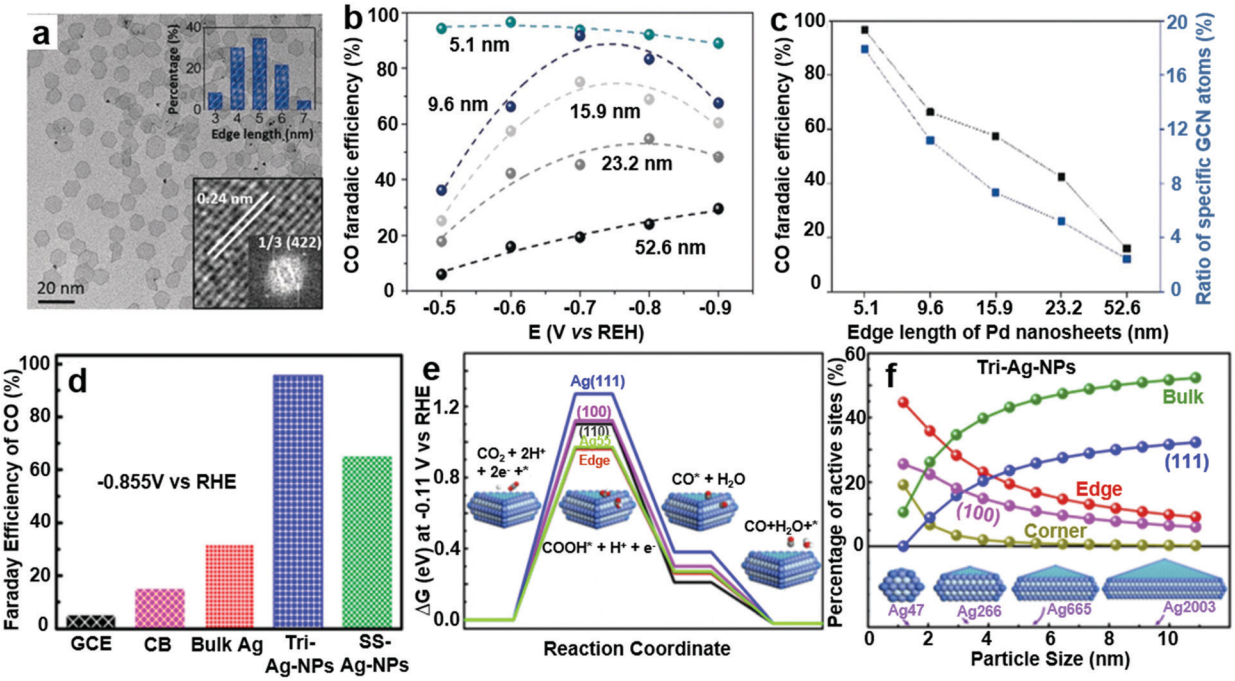

Fig. 11 Different types of 2D metals for CO_2 reduction applications. (a) TEM images of 5.1 nm 2D Pd. Inset shows the Pd edge length distribution and Fourier-transform infrared spectra. (b) LSV of 2D Pd. (c) CO faradaic efficiency of 2D Pd with different edge lengths.[161] Reproduced with permission from © 2018 Wiley-VCH Verlag GmbH & Co. KGaA, Weinheim. (d) CO FEs at fixed potential of −0.855 V with 2D Ag catalyst. (e) Free-energy diagrams for CO_2 reduction to CO on the different facets of 2D Ag catalyst and Ag_{55} cluster at −0.11 V. (f) Active adsorption site density on Tri-Ag-NPs as a function of the particle size.[162] Reproduced with permission from © 2017 American Chemical Society.

also weakened the binding strength of CO on Pd due to the as-built Pd–O–Sn interfaces, which was demonstrated to be critical to improve the electrocatalytic selectivity and stability of Pd catalysts. The hybrid 2D structure enabled multielectron transfer for the selective electroreduction of CO_2 into CH_3OH.[165]

A drastic enhancement in the catalytic activity toward the electroreduction of CO_2 into formate was obtained from 2D Co.[169] Freestanding 2D Co with a thickness of only four atomic layers was synthesized by a ligand-confined growth strategy. The 2D morphology exhibited higher catalytic activity and selectivity toward formate production at lower overpotential than those observed for bulk samples. It was argued that Co atoms confined in the atomic layers could facilitate CO_2 activation by stabilizing the $CO_2^{\bullet-}$ intermediate more effectively than that by their bulk counterpart. The partial oxidation of the atomic layers could further increase the activity and selectivity toward formate production. After partial oxidation, 2D Co showed a stable current density of ~10 mA cm^{-2} for over 40 h, with 90% formate selectivity at overpotential of 0.24 V. Compared with bulk Co, these atomically thin sheets achieved a 260-fold increase in current density. Partially oxidized 2D Co demonstrated further enhanced CO_2 adsorption capacity, which promoted the intermediate reaction.

6.2. Metal oxides

2D metal oxides have also been widely studied as CO_2 reduction electrocatalysts.[168,170,171] Further, 2D nonlayered metal oxides with abundant low-coordinated surface metal cations could serve as the adsorption sites for CO_2 in reduction processes and enhance CO_2 activation. A decrease in thickness can lead to significant increases in active sites and electrical conductivity and therefore improve the electrocatalytic activity. Gao *et al.* demonstrated that 1.72 nm 2D Co_3O_4 exhibited a higher electroreduction CO_2 activity than 3.51 nm 2D Co_3O_4 and its bulk counterpart.[166] The thinner structure endowed 2D Co_3O_4 with a higher fraction of low-coordinated surface Co atoms, which could serve as the main adsorption sites for CO_2 in the reduction processes, thereby ensuring a large amount of CO_2 adsorption that is necessary for the subsequent reduction reactions. DFT calculations revealed that thinner 2D Co_3O_4 had a more dispersed charge density near the Fermi level (Fig. 12a and b), which was beneficial for increasing the electronic conductivity. As a result, 1.72 nm 2D Co_3O_4 had a current density of 0.68 mA cm^{-2} at −0.88 V *vs.* SCE, which was over 1.5 and 20 times higher than that of 3.51 nm 2D Co_3O_4 and the bulk counterpart, respectively (Fig. 12c). The quick electron transport along the 2D ultrathin layer allowed for low corrosion rates and hence led to long-term durability in aqueous electrolytes. Further, 1.72 nm 2D Co_3O_4 showed formate faradaic efficiency of over 60% in 20 h.

Further, 2D nonlayered materials possess abundant exposed surface atoms that can easily escape from the respective lattice to form vacancy-type defects. In oxides, O vacancies can reduce the coordination number of the surface atoms and promote the chemisorption of CO_2 molecules. CO_2 molecules are prone to adsorption at the O vacancies with one oxygen atom of CO_2 situated by bridging the O-vacancy defects, thereby decreasing

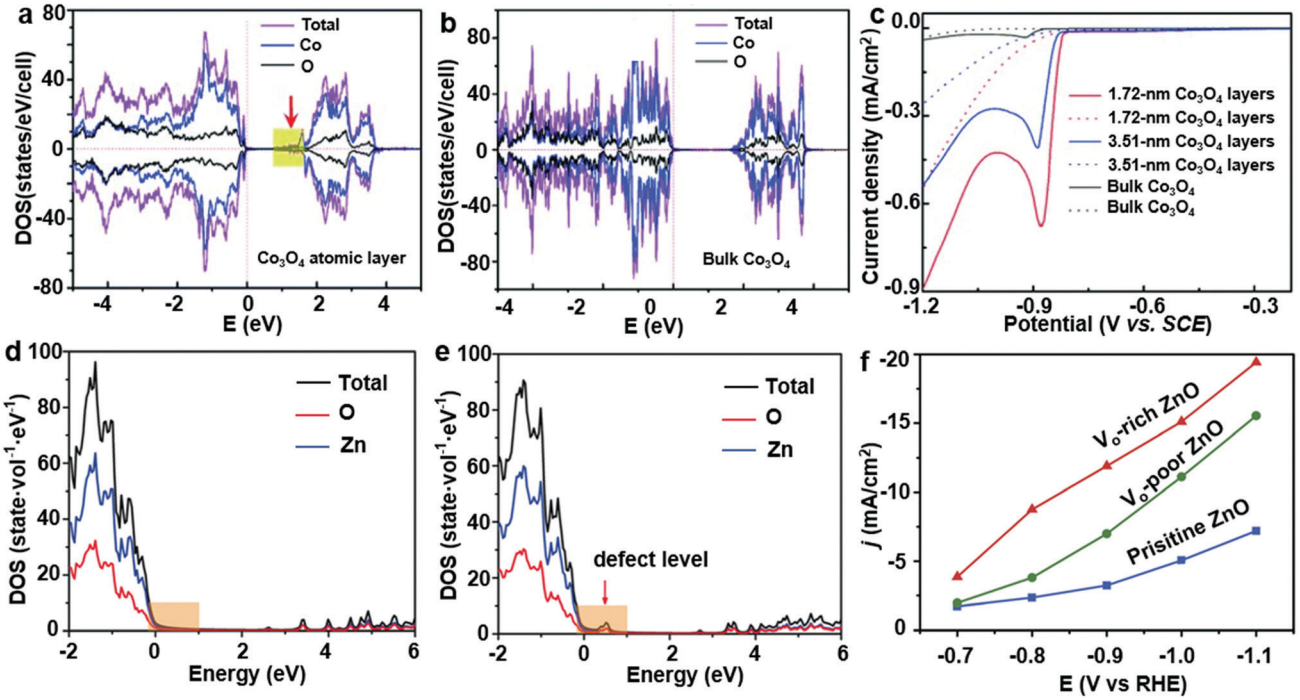

Fig. 12 Different types of 2D metal oxides for CO_2 reduction. Calculated DOS for (a) 2D Co_3O_4 with a thickness of 1.72 nm and (b) bulk Co_3O_4 slab. The yellow-shaded parts represent the increased DOS at the conduction band edges of the Co_3O_4 atomic layer. (c) LSV curves for the electroreduction of CO_2 into formate by 2D Co_3O_4 with different thicknesses in the CO_2-saturated (solid line) and N_2-saturated (dashed line) 0.1 M $KHCO_3$ aqueous solution.[166] Reproduced with permission from © 2016 Wiley-VCH Verlag GmbH & Co. KGaA, Weinheim. Calculated DOSs of (d) 2D ZnO and (e) 2D ZnO with an O vacancy. (f) Total current densities for CO production on the three 2D ZnO materials at the corresponding potential values.[173] Reproduced with permission from © 2018 Wiley-VCH Verlag GmbH & Co. KGaA, Weinheim.

the energy barrier for CO_2 activation.[172] Geng *et al.* developed 2D ZnO rich in O vacancies as efficient catalysts toward CO_2 electrochemical reduction.[173] The O vacancies were introduced by a facile H_2 plasma treatment. DFT calculations demonstrated that the introduction of O vacancies increased the charge density of ZnO at the valence band maximum, resulting in the enhanced activation of CO_2 (Fig. 12d and e). In CO_2 electrochemical reduction, O-deficient 2D ZnO exhibited a current density for CO production of -16.1 mA cm^{-2} with faradaic efficiency of 83% at -1.1 V *vs.* RHE (Fig. 12f). A mechanistic study revealed that O vacancies improved the binding strength of CO_2 and facilitated the activation of CO_2, leading to superior kinetics for CO production. Similarly, Gao *et al.* demonstrated the role of O vacancies confined in Co_3O_4 single-unit-cell layers for CO_2 electroreduction.[167] By comparing the 2D Co_3O_4 with high and low O-vacancy concentrations, it was found that O vacancies facilitated CO_2 adsorption as well as $HCOO^-$ desorption. Additionally, the electrokinetic results demonstrated that proton transfer from HCO_3^- was a rate-determining step. DFT calculations unveiled that O vacancies could lower the rate-limiting activation barrier from 0.51 to 0.40 eV by stabilizing the $HCOO^-$* intermediates, as reflected by the lowered onset potential from 0.81 to 0.78 V and decreased Tafel slope from 48 to 37 mV dec^{-1}. O-Vacancy-rich 2D Co_3O_4 exhibited a current density of 2.7 mA cm^{-2} with ~85% formate selectivity during 40 h tests.

7. Conclusions and perspectives

In this review, we summarized the recent progresses made in emerging 2D nonlayered materials for four representative types of electrocatalytic reactions. Various 2D nonlayered catalysts such as metals, metal oxides, metal chalcogenides, metal nitrides, and metal phosphides were systematically reviewed. We discussed the approaches and mechanisms for modulating the electronic structure in 2D nonlayered materials as an emerging platform for advanced electrocatalysis. By thickness tuning, vacancy engineering, doping, and hybridization, the electronic states of 2D materials could be effectively controlled, thereby leading to significantly improved catalytic performance. Another unique and significant advantage for 2D nonlayered materials is their extremely large ratio between the surface atoms and bulk atoms, which can significantly reduce the mass requirement for precise elements in high-performance electrocatalyst designs. Compared with layered materials, 2D nonlayered materials offer unique performance features toward electrocatalysis. Firstly, 2D nonlayered materials possess numerous low-coordinated atoms at the surface, which are of great benefit for the chemisorption of reactants, enabling highly chemically active surfaces and enhanced catalytic performance. Secondly, the large lattice structure distortion with massive surface dangling bonds modifies the electronic states at the surface, which significantly enhances the electrical conductivity and carrier mobility, enabling faster reaction kinetics.

Thirdly, the structural and electronic properties of 2D nonlayered materials can be tuned by structure and surface engineering, which can further be used to manipulate the surface electronic states for enhanced performances in various catalytic applications.

7.1 HER

HER is the most extensively studied electrocatalytic process using 2D nonlayered materials, and many promising results have been obtained. However, there are still a few big challenges in achieving cost-effective electrocatalysis with catalytic activities matching those of noble metals (*i.e.*, Pt, Pd, and Rh). More research efforts are needed for the controllable design and synthesis of nonlayered materials from earth-abundant elements to realize a higher ratio of exposed surface active sites and well-engineered defects to reach the desired ΔG_H and charge transfer kinetics. Moreover, 2D metal alloys would be a promising new solution for developing low-cost, highly efficient, nonnoble-metal-based HER catalysts due to synergistic effects. Most 2D materials are restricted to strong acidic or alkaline electrolytes for achieving higher HER activities. Electrocatalytic HER in neutral aqueous systems (*e.g.*, seawater) remains a big challenge due to its low conductivity, ion poisoning, and high corrosivity. The intriguing structural and electronic properties of 2D nonlayered materials, as well as various approaches used to control their morphology and electronic structures, could provide a new platform for exploring HER in neutral electrolytes. Furthermore, the lack of long-term stability and durability is a generic problem for nanoscale catalysts. In this regard, selecting appropriate supporting materials to hybridize 2D materials could provide new opportunities to improve the longevity against air oxidation and electrocatalyst collapse.

7.2 OER and ORR

Current research on 2D nonlayered materials for OER and ORR is still far from mature. Due to sluggish kinetics, the efficiency of most of the reported nanoscale catalysts remains insufficient to replace the costly commercial precious-metal-based electrocatalysts (*e.g.*, Pt for ORR and IrO_2 for OER). The main research efforts should be devoted toward either maximizing the atom efficiency of noble-metal-based electrocatalysts or developing high-performance electrocatalysts from earth-abundant materials. Achieving appropriate thermodynamic adsorption energies and kinetic reaction barriers in 2D catalyst design is essential to enhance the catalytic efficiency. The rational design and fine modulation of the electronic structure could be an effective pathway to further enhance the catalytic performance. Possible methods include controlling the thickness, doping and alloying with other elements, and introducing structural heterogeneity. Thus far, the fundamentals of OER and ORR activities are still unclear in most 2D material systems rather than performance demonstrations. *In situ* characterization techniques combined with theoretical computations are highly promising to bring fundamental insights into the thickness and surface-related reaction kinetics, which are essential to build the structure–activity relationships in different material systems.

7.3 CO_2 reduction

Although advances have been made in the electrocatalytic reduction of CO_2, most of the electrocatalysts are still facing low energy efficiency, unsatisfactory selectivity, and poor stability. Moreover, due to the complexity associated with multiple surface adsorption patterns and various reaction products, the fundamental mechanisms and kinetics of CO_2 adsorption, activation, multi-electron transfer, and desorption processes still need a deeper understanding. Practically, costly noble metal catalysts have still been primarily used to achieve the highest efficiency. Currently, many research efforts have been focused on the design and synthesis of cost-effective and stable electrocatalysts that can reduce CO_2 at higher rates at minimum overpotential. Nonlayered materials have been demonstrated to be an excellent choice for CO_2 reduction due to their unique structural and electronic properties. The large amount of low-coordinated metal atoms on the surface of metal or metal oxide 2D materials are favorable for stabilizing $CO_2^{\bullet-}$ intermediates, thereby lowering the overall activation energy barrier and remarkably improving the catalytic activity. The structural modification of 2D nonlayered materials can be an efficient pathway to achieve further enhancement in catalytic performance. Possible research directions include the control of thickness, creating defects and heterogeneous interfaces, and doping and alloying with other elements. The rational control of thickness and defect levels of nonlayered materials could effectively modulate the electron transfer kinetics and further tune the CO_2 reduction activity. It is also promising to explore multinary 2D materials to boost the performances. A combination of theoretical and experimental studies on complex catalytic reaction pathways are desired to aid future catalyst design, particularly from earth-abundant materials that can take advantage of the 2D morphology to convert CO_2 to targeted products at sufficiently high reaction rate and efficiency.

In general, although research on 2D nonlayered materials for advanced electrocatalysis is just in its infancy, this new type of material has already showed great promise in catalyzing many electrochemical redox reactions. In the future, extensive efforts are needed to elucidate the details of the electrocatalysis mechanisms with 2D nonlayered materials, as they currently remain poorly understood. With the help of atomic- and electronic-level mechanistic understandings, together with advanced and scalable synthesis approaches, 2D nonlayered materials can soon evolve into a new group of highly efficient, cost-effective, and sustainable electrocatalysts for a broad range of energy and environmental applications.

Conflicts of interest

There are no conflicts to declare.

Acknowledgements

This work was primarily supported by National Science Foundation DMR-1709025.

Notes and references

1 Y. Dou, L. Zhang, X. Xu, Z. Sun, T. Liao and S. X. Dou, *Chem. Soc. Rev.*, 2017, **46**, 7338–7373.
2 D. L. Duong, S. J. Yun and Y. H. Lee, *ACS Nano*, 2017, **11**, 11803–11830.
3 C. Tan, X. Cao, X.-J. Wu, Q. He, J. Yang, X. Zhang, J. Chen, W. Zhao, S. Han, G.-H. Nam, M. Sindoro and H. Zhang, *Chem. Rev.*, 2017, **117**, 6225–6331.
4 R. Dong, T. Zhang and X. Feng, *Chem. Rev.*, 2018, **118**, 6189–6235.
5 J. Ji, J. Wen, Y. Shen, Y. Lv, Y. Chen, S. Liu, H. Ma and Y. Zhang, *J. Am. Chem. Soc.*, 2017, **139**, 11698–11701.
6 Y. Lv, S. Chen, Y. Shen, J. Ji, Q. Zhou, S. Liu and Y. Zhang, *J. Am. Chem. Soc.*, 2018, **140**, 2801–2804.
7 Z. Zhou, Y. Zhang, Y. Shen, S. Liu and Y. Zhang, *Chem. Soc. Rev.*, 2018, **47**, 2298–2321.
8 D. Han, D. Ni, Q. Zhou, J. Ji, Y. Lv, Y. Shen, S. Liu and Y. Zhang, *Adv. Funct. Mater.*, 2019, **29**, 1905576.
9 P. Giusto, D. Cruz, T. Heil, H. Arazoe, P. Lova, T. Aida, D. Comoretto, M. Patrini and M. Antonietti, *Adv. Mater.*, 2020, **32**, 1908140.
10 S. N. Talapaneni, G. Singh, I. Y. Kim, K. AlBahily, A. A. H. Al-Muhtaseb, A. S. Karakoti, E. Tavakkoli and A. Vinu, *Adv. Mater.*, 2020, **32**, 1904635.
11 Y. Xu, J. Xue, Q. Zhou, Y. Zheng, X. Chen, S. Liu, Y. Shen and Y. Zhang, *Angew. Chem., Int. Ed.*, 2020, **59**, 14498–14503.
12 H. Yang, Z. Wang, S. Liu, Y. Shen and Y. Zhang, *Chin. Chem. Lett.*, 2020, DOI: 10.1016/j.cclet.2020.07.048.
13 Y. Zhang, Y. Song, Y. Shen, K. Chen, Q. Zhou, Y. Lv, H. Yang, E. Xu, S. Liu, L. Liu and Y. Zhang, *CCS Chem.*, 2020, **2**, 1615–1625, DOI: 10.31635/ccschem.20.202000361.
14 T. Zhao, Q. Zhou, Y. Lv, D. Han, K. Wu, L. Zhao, Y. Shen, S. Liu and Y. Zhang, *Angew. Chem., Int. Ed.*, 2020, **59**, 1139–1143.
15 Q. H. Wang, K. Kalantar-Zadeh, A. Kis, J. N. Coleman and M. S. Strano, *Nat. Nanotechnol.*, 2012, **7**, 699–712.
16 W. Tao, N. Kong, X. Ji, Y. Zhang, A. Sharma, J. Ouyang, B. Qi, J. Wang, N. Xie, C. Kang, H. Zhang, O. C. Farokhzad and J. S. Kim, *Chem. Soc. Rev.*, 2019, **48**, 2891–2912.
17 H. Liu, Y. Du, Y. Deng and P. D. Ye, *Chem. Soc. Rev.*, 2015, **44**, 2732–2743.
18 Q. Weng, X. Wang, X. Wang, Y. Bando and D. Golberg, *Chem. Soc. Rev.*, 2016, **45**, 3989–4012.
19 M. Zhao, Y. Huang, Y. Peng, Z. Huang, Q. Ma and H. Zhang, *Chem. Soc. Rev.*, 2018, **47**, 6267–6295.
20 D. Rhodes, S. H. Chae, R. Ribeiro-Palau and J. Hone, *Nat. Mater.*, 2019, **18**, 541–549.
21 Z. Zhang, P. Lin, Q. Liao, Z. Kang, H. Si and Y. Zhang, *Adv. Mater.*, 2019, **31**, 1806411.
22 X. Zhang, Q. Liao, S. Liu, Z. Kang, Z. Zhang, J. Du, F. Li, S. Zhang, J. Xiao, B. Liu, Y. Ou, X. Liu, L. Gu and Y. Zhang, *Nat. Commun.*, 2017, **8**, 15881.
23 L. Gao, Q. Liao, X. Zhang, X. Liu, L. Gu, B. Liu, J. Du, Y. Ou, J. Xiao, Z. Kang, Z. Zhang and Y. Zhang, *Adv. Mater.*, 2020, **32**, 1906646.
24 B. Liu, Q. Liao, X. Zhang, J. Du, Y. Ou, J. Xiao, Z. Kang, Z. Zhang and Y. Zhang, *ACS Nano*, 2019, **13**, 9057–9066.
25 K. S. Novoselov, D. Jiang, F. Schedin, T. J. Booth, V. V. Khotkevich, S. V. Morozov and A. K. Geim, *Proc. Natl. Acad. Sci. U. S. A.*, 2005, **102**, 10451–10453.
26 S. Ida, D. Shiga, M. Koinuma and Y. Matsumoto, *J. Am. Chem. Soc.*, 2008, **130**, 14038–14039.
27 M. Choucair, P. Thordarson and J. A. Stride, *Nat. Nanotechnol.*, 2008, **4**, 30.
28 D. Wei, Y. Liu, Y. Wang, H. Zhang, L. Huang and G. Yu, *Nano Lett.*, 2009, **9**, 1752–1758.
29 W. Strupinski, K. Grodecki, A. Wysmolek, R. Stepniewski, T. Szkopek, P. E. Gaskell, A. Grüneis, D. Haberer, R. Bozek, J. Krupka and J. M. Baranowski, *Nano Lett.*, 2011, **11**, 1786–1791.
30 H. Jin, C. Guo, X. Liu, J. Liu, A. Vasileff, Y. Jiao, Y. Zheng and S.-Z. Qiao, *Chem. Rev.*, 2018, **118**, 6337–6408.
31 J. Di, C. Yan, A. D. Handoko, Z. W. Seh, H. Li and Z. Liu, *Mater. Today*, 2018, **21**, 749–770.
32 J. Di, J. Xiong, H. Li and Z. Liu, *Adv. Mater.*, 2018, **30**, 1704548.
33 M. P. Browne, Z. Sofer and M. Pumera, *Energy Environ. Sci.*, 2019, **12**, 41–58.
34 Y. Zhu, L. Peng, Z. Fang, C. Yan, X. Zhang and G. Yu, *Adv. Mater.*, 2018, **30**, 1706347.
35 F. Wang, J.-H. Seo, G. Luo, M. B. Starr, Z. Li, D. Geng, X. Yin, S. Wang, D. G. Fraser, D. Morgan, Z. Ma and X. Wang, *Nat. Commun.*, 2016, **7**, 10444.
36 C. Schliehe, B. H. Juarez, M. Pelletier, S. Jander, D. Greshnykh, M. Nagel, A. Meyer, S. Foerster, A. Kornowski, C. Klinke and H. Weller, *Science*, 2010, **329**, 550–553.
37 Y. Sun, Z. Sun, S. Gao, H. Cheng, Q. Liu, J. Piao, T. Yao, C. Wu, S. Hu, S. Wei and Y. Xie, *Nat. Commun.*, 2012, **3**, 1057.
38 L. Liang, H. Cheng, F. Lei, J. Han, S. Gao, C. Wang, Y. Sun, S. Qamar, S. Wei and Y. Xie, *Angew. Chem., Int. Ed.*, 2015, **54**, 12004–12008.
39 X. Huang, S. Li, Y. Huang, S. Wu, X. Zhou, S. Li, C. L. Gan, F. Boey, C. A. Mirkin and H. Zhang, *Nat. Commun.*, 2011, **2**, 292.
40 X. Xiao, H. Wang, P. Urbankowski and Y. Gogotsi, *Chem. Soc. Rev.*, 2018, **47**, 8744–8765.
41 F. Wang, Z. Wang, T. A. Shifa, Y. Wen, F. Wang, X. Zhan, Q. Wang, K. Xu, Y. Huang, L. Yin, C. Jiang and J. He, *Adv. Funct. Mater.*, 2017, **27**, 1603254.
42 C. Tan and H. Zhang, *Nat. Commun.*, 2015, **6**, 7873.
43 X. Zhang, Z. Zhang, J. Liang, Y. Zhou, Y. Tong, Y. Wang and X. Wang, *J. Mater. Chem. A*, 2017, **5**, 9702–9708.
44 X. Yin, Y. Shi, Y. Wei, Y. Joo, P. Gopalan, I. Szlufarska and X. Wang, *Langmuir*, 2017, **33**, 7708–7714.
45 Y. Sun, F. Lei, S. Gao, B. Pan, J. Zhou and Y. Xie, *Angew. Chem., Int. Ed.*, 2013, **52**, 10569–10572.
46 G. Yan, Y. Wang, Z. Zhang, Y. Dong, J. Wang, C. Carlos, P. Zhang, Z. Cao, Y. Mao and X. Wang, *Nano-Micro Lett.*, 2020, **12**, 49.
47 H. L. Qin, D. Wang, Z. L. Huang, D. M. Wu, Z. C. Zeng, B. Ren, K. Xu and J. Jin, *J. Am. Chem. Soc.*, 2013, **135**, 12544–12547.

48 M. Zhou, M. Lin, L. Chen, Y. Wang, X. Guo, L. Peng, X. Guo and W. Ding, *Chem. Commun.*, 2015, **51**, 5116–5119.
49 Y. Han, Y. Yan, Z. Wu, Y. Jiang, X. Li, Q. Xu, X. Yang, H. Zhang and D. Yang, *CrystEngComm*, 2018, **20**, 4230–4236.
50 H. Zhao, Y. Zhu, F. Li, R. Hao, S. Wang and L. Guo, *Angew. Chem., Int. Ed.*, 2017, **56**, 8766–8770.
51 X. Yin, Y. Wang, T.-H. Chang, P. Zhang, J. Li, P. Xue, Y. Long, J. L. Shohet, P. M. Voyles, Z. Ma and X. Wang, *Adv. Mater.*, 2020, 2000801.
52 X. Yin, Q. Chen, P. Tian, P. Zhang, Z. Zhang, P. M. Voyles and X. Wang, *Chem. Mater.*, 2018, **30**, 3308–3314.
53 F. Wang, Y. Yu, X. Yin, P. Tian and X. Wang, *J. Mater. Chem. A*, 2017, **5**, 9060–9066.
54 Y. Wang, Y. Shi, Z. Zhang, C. Carlos, C. Zhang, K. Bhawnani, J. Li, J. Wang, P. M. Voyles, I. Szlufarska and X. Wang, *Chem. Mater.*, 2019, **31**, 9040–9048.
55 M. Lyu, Y. Liu, Y. Zhi, C. Xiao, B. Gu, X. Hua, S. Fan, Y. Lin, W. Bai, W. Tong, Y. Zou, B. Pan, B. Ye and Y. Xie, *J. Am. Chem. Soc.*, 2015, **137**, 15043–15048.
56 Y. Liu, C. Xiao, P. Huang, M. Cheng and Y. Xie, *Chem*, 2018, **4**, 1263–1283.
57 F. Lei, Y. Sun, K. Liu, S. Gao, L. Liang, B. Pan and Y. Xie, *J. Am. Chem. Soc.*, 2014, **136**, 6826–6829.
58 Y. Liu, H. Cheng, M. Lyu, S. Fan, Q. Liu, W. Zhang, Y. Zhi, C. Wang, C. Xiao, S. Wei, B. Ye and Y. Xie, *J. Am. Chem. Soc.*, 2014, **136**, 15670–15675.
59 Y. Sun, Q. Liu, S. Gao, H. Cheng, F. Lei, Z. Sun, Y. Jiang, H. Su, S. Wei and Y. Xie, *Nat. Commun.*, 2013, **4**, 2899.
60 Y. Sun, S. Gao, F. Lei, J. Liu, L. Liang and Y. Xie, *Chem. Sci.*, 2014, **5**, 3976–3982.
61 Y. Liu, L. Liang, C. Xiao, X. Hua, Z. Li, B. Pan and Y. Xie, *Adv. Energy Mater.*, 2016, **6**, 1600437.
62 X. Yin, Y. Wang, R. Jacobs, Y. Shi, I. Szlufarska, D. Morgan and X. Wang, *Nano Lett.*, 2019, **19**, 7085–7092.
63 L. Xu, Q. Jiang, Z. Xiao, X. Li, J. Huo, S. Wang and L. Dai, *Angew. Chem., Int. Ed.*, 2016, **55**, 5277–5281.
64 H. Zhang, Q. Liu, J. Xu, L. Wei, Q. Liu and X. Kong, *Inorg. Chem.*, 2019, **58**, 8267–8270.
65 F. Lei, L. Zhang, Y. Sun, L. Liang, K. Liu, J. Xu, Q. Zhang, B. Pan, Y. Luo and Y. Xie, *Angew. Chem., Int. Ed.*, 2015, **54**, 9266–9270.
66 Y. Liu, X. Hua, C. Xiao, T. Zhou, P. Huang, Z. Guo, B. Pan and Y. Xie, *J. Am. Chem. Soc.*, 2016, **138**, 5087–5092.
67 H. Duan, N. Yan, R. Yu, C.-R. Chang, G. Zhou, H.-S. Hu, H. Rong, Z. Niu, J. Mao, H. Asakura, T. Tanaka, P. J. Dyson, J. Li and Y. Li, *Nat. Commun.*, 2014, **5**, 3093.
68 X. Huang, S. Tang, X. Mu, Y. Dai, G. Chen, Z. Zhou, F. Ruan, Z. Yang and N. Zheng, *Nat. Nanotechnol.*, 2011, **6**, 28–32.
69 M. Luo, Y. Yang, Y. Sun, Y. Qin, C. Li, Y. Li, M. Li, S. Zhang, D. Su and S. Guo, *Mater. Today*, 2019, **23**, 45–56.
70 X. Kong, K. Xu, C. Zhang, J. Dai, S. Norooz Oliaee, L. Li, X. Zeng, C. Wu and Z. Peng, *ACS Catal.*, 2016, **6**, 1487–1492.
71 Y. Kuang, G. Feng, P. Li, Y. Bi, Y. Li and X. Sun, *Angew. Chem., Int. Ed.*, 2016, **55**, 693–697.
72 L. Dai, Y. Zhao, Q. Qin, X. Zhao, C. Xu and N. Zheng, *ChemNanoMat*, 2016, **2**, 776–780.
73 Q. Zhang, P. Li, D. Zhou, Z. Chang, Y. Kuang and X. Sun, *Small*, 2017, **13**, 1701648.
74 A. Mahmood, H. Lin, N. Xie and X. Wang, *Chem. Mater.*, 2017, **29**, 6329–6335.
75 X. Zhao, L. Dai, Q. Qin, F. Pei, C. Hu and N. Zheng, *Small*, 2017, **13**, 1602970.
76 H. Liang, L. Li, F. Meng, L. Dang, J. Zhuo, A. Forticaux, Z. Wang and S. Jin, *Chem. Mater.*, 2015, **27**, 5702–5711.
77 X. Long, G. Li, Z. Wang, H. Zhu, T. Zhang, S. Xiao, W. Guo and S. Yang, *J. Am. Chem. Soc.*, 2015, **137**, 11900–11903.
78 L. Ma, Y. Hu, R. Chen, G. Zhu, T. Chen, H. Lv, Y. Wang, J. Liang, H. Liu, C. Yan, H. Zhu, Z. Tie, Z. Jin and J. Liu, *Nano Energy*, 2016, **24**, 139–147.
79 F. Wang, Y. Li, T. A. Shifa, K. Liu, F. Wang, Z. Wang, P. Xu, Q. Wang and J. He, *Angew. Chem., Int. Ed.*, 2016, **55**, 6919–6924.
80 C. Zhang, Y. Shi, Y. Yu, Y. Du and B. Zhang, *ACS Catal.*, 2018, **8**, 8077–8083.
81 H. Wu, X. Lu, G. Zheng and G. W. Ho, *Adv. Energy Mater.*, 2018, **8**, 1702704.
82 D. Gao, J. Zhang, T. Wang, W. Xiao, K. Tao, D. Xue and J. Ding, *J. Mater. Chem. A*, 2016, **4**, 17363–17369.
83 H. Jin, X. Liu, A. Vasileff, Y. Jiao, Y. Zhao, Y. Zheng and S.-Z. Qiao, *ACS Nano*, 2018, **12**, 12761–12769.
84 Z. Pu, Q. Liu, P. Jiang, A. M. Asiri, A. Y. Obaid and X. Sun, *Chem. Mater.*, 2014, **26**, 4326–4329.
85 X. Wang, Y. V. Kolen'ko, X.-Q. Bao, K. Kovnir and L. Liu, *Angew. Chem., Int. Ed.*, 2015, **54**, 8188–8192.
86 X.-D. Wang, Y.-F. Xu, H.-S. Rao, W.-J. Xu, H.-Y. Chen, W.-X. Zhang, D.-B. Kuang and C.-Y. Su, *Energy Environ. Sci.*, 2016, **9**, 1468–1475.
87 Z. Pu, S. Wei, Z. Chen and S. Mu, *Appl. Catal., B*, 2016, **196**, 193–198.
88 L. Zhou, M. Shao, J. Li, S. Jiang, M. Wei and X. Duan, *Nano Energy*, 2017, **41**, 583–590.
89 C. Zhang, Y. Huang, Y. Yu, J. Zhang, S. Zhuo and B. Zhang, *Chem. Sci.*, 2017, **8**, 2769–2775.
90 H. Li, X. Zhao, H. Liu, S. Chen, X. Yang, C. Lv, H. Zhang, X. She and D. Yang, *Small*, 2018, **14**, 1802824.
91 T. Li, H. Jin, Z. Liang, L. Huang, Y. Lu, H. Yu, Z. Hu, J. Wu, B. Y. Xia, G. Feng and J. Zhou, *Nanoscale*, 2018, **10**, 6844–6849.
92 X. Zhang, J. Ji, Q. Yang, L. Zhao, Q. Yuan, Y. Hao, P. Jin and L. Feng, *ChemCatChem*, 2019, **58**, 4774–4781.
93 X. Liu, B. Wei, R. Su, C. Zhao, D. Dai, X. Ma and L. Xu, *Energy Technol.*, 2019, 1900021.
94 A. Kumatani, C. Miura, H. Kuramochi, T. Ohto, M. Wakisaka, Y. Nagata, H. Ida, Y. Takahashi, K. Hu, S. Jeong, J.-I. Fujita, T. Matsue and Y. Ito, *Adv. Sci.*, 2019, **6**, 1900119.
95 Z. Pei, J. Gu, Y. Wang, Z. Tang, Z. Liu, Y. Huang, Y. Huang, J. Zhao, Z. Chen and C. Zhi, *ACS Nano*, 2017, **11**, 6004–6014.
96 Y. Yin, J. Han, Y. Zhang, X. Zhang, P. Xu, Q. Yuan, L. Samad, X. Wang, Y. Wang, Z. Zhang, P. Zhang, X. Cao, B. Song and S. Jin, *J. Am. Chem. Soc.*, 2016, **138**, 7965–7972.
97 Y. Sun, X. Zhang, B. Mao and M. Cao, *Chem. Commun.*, 2016, **52**, 14266–14269.

98 W. Chen, J. Gu, Y. Du, F. Song, F. Bu, J. Li, Y. Yuan, R. Luo, Q. Liu and D. Zhang, *Adv. Funct. Mater.*, 2020, **30**, 2000551.
99 M. M. Jaksic and J. M. Jaksic, *Electrochim. Acta*, 1994, **39**, 1695–1714.
100 M. Metikoš-Huković and A. Jukić, *Electrochim. Acta*, 2000, **45**, 4159–4170.
101 D. Zhang, H. Zhao, B. Huang, B. Li, H. Li, Y. Han, Z. Wang, X. Wu, Y. Pan, Y. Sun, X. Sun, J. Lai and L. Wang, *ACS Cent. Sci.*, 2019, **5**, 1991–1997.
102 X. Wang, R. Su, H. Aslan, J. Kibsgaard, S. Wendt, L. Meng, M. Dong, Y. Huang and F. Besenbacher, *Nano Energy*, 2015, **12**, 9–18.
103 T. F. Jaramillo, K. P. Jørgensen, J. Bonde, J. H. Nielsen, S. Horch and I. Chorkendorff, *Science*, 2007, **317**, 100–102.
104 B. Song, K. Li, Y. Yin, T. Wu, L. Dang, M. Cabán-Acevedo, J. Han, T. Gao, X. Wang, Z. Zhang, J. R. Schmidt, P. Xu and S. Jin, *ACS Catal.*, 2017, **7**, 8549–8557.
105 J. Xie and Y. Xie, *Chem. – Eur. J.*, 2016, **22**, 3588–3598.
106 H.-P. Guo, B.-Y. Ruan, W.-B. Luo, J. Deng, J.-Z. Wang, H.-K. Liu and S.-X. Dou, *ACS Catal.*, 2018, **8**, 9686–9696.
107 P. Jiang, Q. Liu and X. Sun, *Nanoscale*, 2014, **6**, 13440–13445.
108 Y. Shi and B. Zhang, *Chem. Soc. Rev.*, 2016, **45**, 1529–1541.
109 Y. Zhao, X. Jia, G. Chen, L. Shang, G. I. N. Waterhouse, L.-Z. Wu, C.-H. Tung, D. O'Hare and T. Zhang, *J. Am. Chem. Soc.*, 2016, **138**, 6517–6524.
110 S. M. Pawar, B. S. Pawar, B. Hou, J. Kim, A. T. Aqueel Ahmed, H. S. Chavan, Y. Jo, S. Cho, A. I. Inamdar, J. L. Gunjakar, H. Kim, S. Cha and H. Im, *J. Mater. Chem. A*, 2017, **5**, 12747–12751.
111 Y. Dou, T. Liao, Z. Ma, D. Tian, Q. Liu, F. Xiao, Z. Sun, J. Ho Kim and S. Xue Dou, *Nano Energy*, 2016, **30**, 267–275.
112 Y. Huang, X. Zhao, F. Tang, X. Zheng, W. Cheng, W. Che, F. Hu, Y. Jiang, Q. Liu and S. Wei, *J. Mater. Chem. A*, 2018, **6**, 3202–3210.
113 L. Xu, Z. Wang, J. Wang, Z. Xiao, X. Huang, Z. Liu and S. Wang, *Nanotechnology*, 2017, **28**, 165402.
114 P. Tian, Y. Yu, X. Yin and X. Wang, *Nanoscale*, 2018, **10**, 5054–5059.
115 J. Bao, X. Zhang, B. Fan, J. Zhang, M. Zhou, W. Yang, X. Hu, H. Wang, B. Pan and Y. Xie, *Angew. Chem., Int. Ed.*, 2015, **54**, 7399–7404.
116 Y. Li, F.-M. Li, X.-Y. Meng, S.-N. Li, J.-H. Zeng and Y. Chen, *ACS Catal.*, 2018, **8**, 1913–1920.
117 S. Jin, *ACS Energy Lett.*, 2017, **2**, 1937–1938.
118 L. Peng, S. S. A. Shah and Z. Wei, *Chin. J. Catal.*, 2018, **39**, 1575–1593.
119 H. Liu, C.-Y. Xu, Y. Du, F.-X. Ma, Y. Li, J. Yu and L. Zhen, *Sci. Rep.*, 2019, **9**, 1951.
120 R. Souleymen, Z. Wang, C. Qiao, M. Naveed and C. Cao, *J. Mater. Chem. A*, 2018, **6**, 7592–7607.
121 Y. Liu, C. Xiao, M. Lyu, Y. Lin, W. Cai, P. Huang, W. Tong, Y. Zou and Y. Xie, *Angew. Chem., Int. Ed.*, 2015, **54**, 11231–11235.
122 S. Zhao, Y. Wang, Q. Zhang, Y. Li, L. Gu, Z. Dai, S. Liu, Y.-Q. Lan, M. Han and J. Bao, *Inorg. Chem. Front.*, 2016, **3**, 1501–1509.
123 Y. Li, J. Yin, L. An, M. Lu, K. Sun, Y.-Q. Zhao, D. Gao, F. Cheng and P. Xi, *Small*, 2018, **14**, 1801070.
124 R. Wei, M. Fang, G. Dong, C. Lan, L. Shu, H. Zhang, X. Bu and J. C. Ho, *ACS Appl. Mater. Interfaces*, 2018, **10**, 7079–7086.
125 L. Zhuang, L. Ge, Y. Yang, M. Li, Y. Jia, X. Yao and Z. Zhu, *Adv. Mater.*, 2017, **29**, 1606793.
126 L. Zhuang, Y. Jia, T. He, A. Du, X. Yan, L. Ge, Z. Zhu and X. Yao, *Nano Res.*, 2018, **11**, 3509–3518.
127 Y. Xu, B. Li, S. Zheng, P. Wu, J. Zhan, H. Xue, Q. Xu and H. Pang, *J. Mater. Chem. A*, 2018, **6**, 22070–22076.
128 S. Zhao, Y. Wang, J. Dong, C.-T. He, H. Yin, P. An, K. Zhao, X. Zhang, C. Gao, L. Zhang, J. Lv, J. Wang, J. Zhang, A. M. Khattak, N. A. Khan, Z. Wei, J. Zhang, S. Liu, H. Zhao and Z. Tang, *Nat. Energy*, 2016, **1**, 16184.
129 M. Qin, S. Li, Y. Zhao, C.-Y. Lao, Z. Zhang, L. Liu, F. Fang, H. Wu, B. Jia, Z. Liu, W. Wang, Y. Liu and X. Qu, *Adv. Energy Mater.*, 2019, **9**, 1803060.
130 J. Wu, M. Liu, K. Chatterjee, K. P. Hackenberg, J. Shen, X. Zou, Y. Yan, J. Gu, Y. Yang, J. Lou and P. M. Ajayan, *Adv. Mater. Interfaces*, 2016, **3**, 1500669.
131 J. Tian, Q. Liu, A. M. Asiri, K. A. Alamry and X. Sun, *ChemSusChem*, 2014, **7**, 2125–2130.
132 Z. Liu, Z. Zhao, Y. Wang, S. Dou, D. Yan, D. Liu, Z. Xia and S. Wang, *Adv. Mater.*, 2017, **29**, 1606207.
133 X. Ren, J. Zhou, X. Qi, Y. Liu, Z. Huang, Z. Li, Y. Ge, S. C. Dhanabalan, J. S. Ponraj, S. Wang, J. Zhong and H. Zhang, *Adv. Energy Mater.*, 2017, **7**, 1700396.
134 J. Suntivich, K. J. May, H. A. Gasteiger, J. B. Goodenough and Y. Shao-Horn, *Science*, 2011, **334**, 1383.
135 H. Tao, Y. Gao, N. Talreja, F. Guo, J. Texter, C. Yan and Z. Sun, *J. Mater. Chem. A*, 2017, **5**, 7257–7284.
136 D. Mukherjee and S. Sampath, *2D Inorganic Materials beyond Graphene*, World Scientific, 2016, pp. 103–136.
137 G. J. K. Acres, J. C. Frost, G. A. Hards, R. J. Potter, T. R. Ralph, D. Thompsett, G. T. Burstein and G. J. Hutchings, *Catal. Today*, 1997, **38**, 393–400.
138 J. A. Keith, G. Jerkiewicz and T. Jacob, *ChemPhysChem*, 2010, **11**, 2779–2794.
139 D. C. Higgins, R. Wang, M. A. Hoque, P. Zamani, S. Abureden and Z. Chen, *Nano Energy*, 2014, **10**, 135–143.
140 A. W. Marc Koper, *Fuel Cell Catalysis: A Surface Science Approach*, John Wiley & Sons Inc., New York, 2009.
141 J. Zhang, *PEM Fuel Cell Electrocatalysts and Catalyst Layers: Fundamentals and Applications*, Springer, New York, 2008.
142 W. Wang, Y. Zhao and Y. Ding, *Nanoscale*, 2015, **7**, 11934–11939.
143 M. K. Debe, *Nature*, 2012, **486**, 43–51.
144 H.-Y. Chen, M.-X. Jin, L. Zhang, A.-J. Wang, J. Yuan, Q.-L. Zhang and J.-J. Feng, *J. Colloid Interface Sci.*, 2019, **543**, 1–8.
145 W. Liu, J. Bao, L. Xu, M. Guan, Z. Wang, J. Qiu, Y. Huang, J. Xia, Y. Lei and H. Li, *Appl. Surf. Sci.*, 2019, **478**, 552–559.
146 J. Bao, Z. Wang, W. Liu, L. Xu, F. Lei, J. Xie, Y. Zhao, Y. Huang, M. Guan and H. Li, *J. Alloys Compd.*, 2018, **764**, 565–573.
147 Y. Wang, J. Li and Z. Wei, *J. Mater. Chem. A*, 2018, **6**, 8194–8209.

148 J. Lai, F. Lin, Y. Tang, P. Zhou, Y. Chao, Y. Zhang and S. Guo, *Adv. Energy Mater.*, 2019, **9**, 1800684.
149 J. Jiang, S. Lu, H. Gao, X. Zhang and H.-Q. Yu, *Nano Energy*, 2016, **27**, 526–534.
150 Z. Xia, J. Fang, X. Zhang, L. Fan, A. J. Barlow, T. Lin, S. Wang, G. G. Wallace, G. Sun and X. Wang, *Appl. Catal., B*, 2019, **245**, 389–398.
151 T. Maiyalagan, K. A. Jarvis, S. Therese, P. J. Ferreira and A. Manthiram, *Nat. Commun.*, 2014, **5**, 3949.
152 D.-N. Pei, L. Gong, A.-Y. Zhang, X. Zhang, J.-J. Chen, Y. Mu and H.-Q. Yu, *Nat. Commun.*, 2015, **6**, 8696.
153 H. Liu, Y. Zheng, G. Wang and S. Z. Qiao, *Adv. Energy Mater.*, 2015, **5**, 1401186.
154 A. Zhang, R. He, H. Li, Y. Chen, T. Kong, K. Li, H. Ju, J. Zhu, W. Zhu and J. Zeng, *Angew. Chem., Int. Ed.*, 2018, **57**, 10954–10958.
155 D. D. Zhu, J. L. Liu and S. Z. Qiao, *Adv. Mater.*, 2016, **28**, 3423–3452.
156 B. A. Rosen, A. Salehi-Khojin, M. R. Thorson, W. Zhu, D. T. Whipple, P. J. A. Kenis and R. I. Masel, *Science*, 2011, **334**, 643–644.
157 W. Zhu, Y.-J. Zhang, H. Zhang, H. Lv, Q. Li, R. Michalsky, A. A. Peterson and S. Sun, *J. Am. Chem. Soc.*, 2014, **136**, 16132–16135.
158 D. Gao, H. Zhou, J. Wang, S. Miao, F. Yang, G. Wang, J. Wang and X. Bao, *J. Am. Chem. Soc.*, 2015, **137**, 4288–4291.
159 C.-Y. Lee, Y. Zhao, C. Wang, D. R. G. Mitchell and G. G. Wallace, *Sustainable Energy Fuels*, 2017, **1**, 1023–1027.
160 F. Quan, D. Zhong, H. Song, F. Jia and L. Zhang, *J. Mater. Chem. A*, 2015, **3**, 16409–16413.
161 W. Zhu, L. Zhang, P. Yang, C. Hu, Z. Luo, X. Chang, Z.-J. Zhao and J. Gong, *Angew. Chem., Int. Ed.*, 2018, **130**, 11718–11722.
162 S. Liu, H. Tao, L. Zeng, Q. Liu, Z. Xu, Q. Liu and J.-L. Luo, *J. Am. Chem. Soc.*, 2017, **139**, 2160–2163.
163 F. Lei, W. Liu, Y. Sun, J. Xu, K. Liu, L. Liang, T. Yao, B. Pan, S. Wei and Y. Xie, *Nat. Commun.*, 2016, **7**, 12697.
164 L. Dai, Q. Qin, P. Wang, X. Zhao, C. Hu, P. Liu, R. Qin, M. Chen, D. Ou, C. Xu, S. Mo, B. Wu, G. Fu, P. Zhang and N. Zheng, *Sci. Adv.*, 2017, **3**, e1701069.
165 W. Zhang, Q. Qin, L. Dai, R. Qin, X. Zhao, X. Chen, D. Ou, J. Chen, T. T. Chuong, B. Wu and N. Zheng, *Angew. Chem., Int. Ed.*, 2018, **57**, 9475–9479.
166 S. Gao, X. Jiao, Z. Sun, W. Zhang, Y. Sun, C. Wang, Q. Hu, X. Zu, F. Yang, S. Yang, L. Liang, J. Wu and Y. Xie, *Angew. Chem., Int. Ed.*, 2016, **128**, 708–712.
167 S. Gao, Z. Sun, W. Liu, X. Jiao, X. Zu, Q. Hu, Y. Sun, T. Yao, W. Zhang, S. Wei and Y. Xie, *Nat. Commun.*, 2017, **8**, 14503.
168 F. Li, L. Chen, G. P. Knowles, D. R. MacFarlane and J. Zhang, *Angew. Chem., Int. Ed.*, 2017, **56**, 505–509.
169 S. Gao, Y. Lin, X. Jiao, Y. Sun, Q. Luo, W. Zhang, D. Li, J. Yang and Y. Xie, *Nature*, 2016, **529**, 68.
170 Z. Chen, K. Mou, X. Wang and L. Liu, *Angew. Chem., Int. Ed.*, 2018, **57**, 12790–12794.
171 H. Dong, L. Zhang, L. Li, W. Deng, C. Hu, Z.-J. Zhao and J. Gong, *Small*, 2019, **15**, 1900289.
172 Z. Sun, T. Ma, H. Tao, Q. Fan and B. Han, *Chem*, 2017, **3**, 560–587.
173 Z. Geng, X. Kong, W. Chen, H. Su, Y. Liu, F. Cai, G. Wang and J. Zeng, *Angew. Chem., Int. Ed.*, 2018, **130**, 6162–6167.

